

Ionization and feedback in Ly α halos around two radio galaxies at $z \sim 2.5$ ^{*}

S. G. Morais¹, A. Humphrey², M. Villar-Martín^{3,4}, P. Lagos², M. Moyano^{5,6},
R. Overzier⁷, S. di Serego Alighieri⁸, J. Vernet⁹, C. A. C. Fernandes⁷

¹ Faculdade de Ciências da Universidade do Porto, Rua do Campo Alegre, 4150-007 Porto, Portugal

² Instituto de Astrofísica e Ciências do Espaço, CAUP, Rua das Estrelas, 4150-762 Porto, Portugal

³ Centro de Astrobiología (INTA-CSIC), Ctra de Torrejón a Ajalvir, km 4, E-28850 Torrejón de Ardoz, Madrid, Spain

⁴ Astro-UAM, UAM, Unidad Asociada CSIC, Facultad de Ciencias, Campus de Cantoblanco, E-28049 Madrid, Spain

⁵ Observatorio Astronómico de Córdoba, Universidad Nacional de Córdoba, Argentina

⁶ Facultad de Matemática, Astronomía y Física, Universidad Nacional de Córdoba, Argentina

⁷ Observatório Nacional, Rua José Cristino, 77. CEP 20921-400, São Cristóvão, Rio de Janeiro-RJ, Brazil

⁸ INAF - Osservatorio Astrofisico di Arcetri, Largo E. Fermi 5, 50125 Firenze, Italy

⁹ European Southern Observatory, Karl Schwarzschild Strasse 2, 85748 Garching bei München, Germany

24 May 2021

ABSTRACT

We present new spectroscopic observations of two high redshift radio galaxies, TXS 0211-122 ($z=2.34$) and TXS 0828+193 ($z=2.57$), known to be associated with large Ly α halos. The observations were taken with the slits placed perpendicularly to the radio axis. With access to pre-existing Keck II observations taken with the slit placed along the radio axis we are able to compare the properties of the gas in different regions of the galaxies.

In both objects we detect spatially extended Ly α emission perpendicularly to the radio axis. In TXS 0211-122, the flux and velocity profiles of Ly α are strongly affected by HI absorption/scattering. In line with previous studies, we find evidence for outflowing gas along the radio axis which may be the result of jet-gas interactions. In the slit oriented perpendicularly to the radio axis we find less perturbed gas kinematics, suggesting outflows of ionized gas in this object are focused along the radio jet axis. Additionally, we find evidence for a giant, UV-emitting arc or shell-like structure surrounding the radio galaxy Ly α halo, possibly resulting from feedback activity.

In TXS 0828+193 a large Ly α halo (~ 56 kpc) is detected perpendicularly to the radio axis. Along both slit position angles we find evidence for outflowing gas, which we argue is part of an approximately spherical, expanding shell or bubble of gas powered by feedback activity in the central regions of the galaxy. Our results suggest a diversity in the spatial distribution of ionized outflows in powerful radio galaxies at $z \sim 2.5$.

Key words: galaxy: formation – high redshift radio galaxies – Ly α halos - outflows

1 INTRODUCTION

High redshift radio galaxies ($z > 2$, hereinafter HzRGs) are useful for understanding the evolution of massive galaxies. They are amongst the largest, most massive and most luminous objects at any epoch (e.g. Jarvis et al. 2001a,b; De Breuck et al. 2002; Rocca-Volmerange et al. 2004). Near-IR and HST imaging of radio galaxies between redshifts 2 and 3 reveal clumpy morphologies, as expected if galaxies are forming through mergers and in agreement with hierarchi-

cal models of galaxy evolution (e.g. Dubinski 1998). They are often found in dense cluster-type regions (e.g. McCarthy 1993; Pentericci et al. 2000; Venemans et al. 2004; Galametz et al. 2012; Mayo et al. 2012; Wylezalek et al. 2013; Dannerbauer et al. 2014). They are believed to be the progenitors of massive elliptical and cD galaxies (e.g. Pentericci et al. 1999; Miley & De Breuck 2008; Adams et al. 2009; Hatch et al. 2009) since it appears that most massive galaxies undergo a phase of radio-loudness during their formation (e.g. Willott et al. 2001).

^{*} Based on observations carried out with the GTC as part of the observing proposal 2-GTC2/11BIACMEX.

Many powerful HzRGs are embedded in large (\sim sev-

eral 10s and up to 200 kpc) luminous Ly α ¹ nebulae (van Ojik et al. 1997; Villar-Martín et al. 2003; Reuland et al. 2003) which have clumpy, irregular morphologies (e.g. Reuland et al. 2003), and are often aligned with the radio source axis (McCarthy et al. 1987, 1995). Alignment between the radio jets and CO(1-0) has also been found (e.g. Klamer et al. 2004; Nesvadba et al. 2009; Emonts et al. 2014).

The main ionizing mechanism in the nebulae seems to be photoionization from Active Galactic Nuclei (hereinafter AGN, e.g. Fosbury et al. 1982), however other mechanisms may also make some contribution: photoionization from stars (e.g. Villar-Martín et al. 2007), photoionization by X-rays emitted by shocked warm gas and collisional excitation from shocks (e.g. Bicknell et al. 2000).

Extended HI absorbers are often found associated with HzRGs. van Ojik et al. (1997) discovered that 90% of HzRGs with small radio sources (<50 kpc) show associated absorption systems while only 25% of HzRGs with larger radio sources had associated HI absorbers. In a few cases, absorption features are also observed in metal lines, such as CIV (Binette et al. 2000; Jarvis et al. 2003). These absorption lines are thought to be formed in cold/warm gas between the emission source and the observer. The observed properties of this absorbing gas suggests that it is part of a super shell of gas with a radius larger than 50 kpc, that is expanding out of the host galaxy (Binette et al. 2000; Humphrey et al. 2008b; Swinbank et al. 2015). As such, they hold important clues about the mass assembly, feedback, and dispersion of metals through galaxies and the intergalactic medium.

The origin, gas distribution, chemical composition and the source of ionization of the gas in the extended Ly α halos are still unclear. Ly α halos may provide important information about the early stages of the formation of massive elliptical galaxies therefore the study of their properties is essential to determine how hosts of powerful radio galaxies form and evolve. Numerous spectroscopic studies of HzRGs have been performed using the long-slit technique. In most cases the slit was aligned with the radio structures (e.g. Legrand et al. 1997; Vernet et al. 2001; Villar-Martín et al. 2003). This is the region where the impact of jet-gas interactions and the ionizing radiation of the AGN are likely to be strongest. In this paper we use long-slit spectra to study the properties of the regions far from the radio jets, outside the ionizing beams of the AGN, with the goal of better understanding the nature and origins of the Ly α halos. This gas traces the properties of the reservoir within which the radio galaxies are embedded, without the distortion produced by the radio structures and/or the excitation by the hard ionizing radiation field of the quasar.

This paper is organized as follows. Section 2 summarizes the results obtained for TXS 0211-122 and TXS 0828+193 in previous works. The observations and data reduction are described in Section 3. In Section 4 the photoionization models used in this work are presented. In Section 5 the observational results for TXS 0211-122 and TXS 0828+193 are presented, and analyzed. In Section 6 the results are discussed.

¹ In the interest of simplicity, we refer to the lines Ly α λ 1216, HeII λ 1640 and the doublets NV λ λ 1240, CIV λ λ 1549 and CIII] λ λ 1909 as Ly α , HeII, NV, CIV and CIII].

Finally, we summarise our main results and final conclusions in Section 7.

A flat universe with $\Omega_{\Lambda}=0.73$, $\Omega_m=0.27$ and $H_0=71$ km s⁻¹ Mpc⁻¹ is adopted in this paper. Using this cosmology 1'' corresponds to 8.295 kpc at $z=2.34$ (TXS 0211-122), and to 8.144 kpc at $z=2.57$ (TXS 0828+193).

2 OVERVIEW OF OUR SAMPLE OF GALAXIES

TXS 0211-122 and TXS 0828+193 belong to the Texas Sky Survey catalogue (Douglas et al. 1980), a catalog containing low-frequency radio sources. They were first selected as high redshift candidates on the basis of their ultra-steep radio spectrum (USS). Optical identification and determination of the redshift of these objects was performed by Röttgering (1993) confirming that they are high redshift radio galaxies.

2.1 TXS 0211-122

TXS 0211-122 is a powerful radio source at $z=2.34$. It has a radio flux at 8.2 GHz of 24 mJy (Röttgering 1993), a very large radio structure (\sim 135 kpc, Carilli et al. 1997) and an optical R-band magnitude of 22.7 (Carilli et al. 1997). De Breuck et al. (2010) derived a maximum stellar mass of the host of this radio galaxy of $<1.45 \times 10^{11} M_{\odot}$.

The radio structure consists of a bright core and a smaller clump. A jet extends from the core towards the south, bends and reaches the eastern lobe (Pentericci et al. 1999). Pentericci et al. (1999) found that the UV continuum emission of this object is aligned with the axis of the radio source. This radio galaxy is associated with an extended Ly α (\sim 110 kpc), CIV and HeII nebula (van Ojik et al. 1994; Villar-Martín et al. 2003), and with a ≥ 100 kpc scale neutral hydrogen (HI) absorbing structure (van Ojik et al. 1994).

van Ojik et al. (1994) found that the Ly α emission is weak when compared to higher ionization lines and that the line-emitting gas is overabundant in nitrogen. They concluded that the galaxy is undergoing a massive starburst which would produce the dust necessary to absorb the Ly α emission and that the enhancement of nitrogen could be due to photoionization or shocks.

Villar-Martín et al. (2003) and Humphrey et al. (2006, 2007a) found a clear difference in kinematics between the gas inside (FWHM \sim 700 km s⁻¹) and outside (FWHM \leq 400 km s⁻¹) the radio structures. The authors propose that the inner gas is in outflow triggered by the interaction between the radio structures and the ambient gas, while the outer, more quiescent gas is in the process of infall.

This source has a high rest-frame UV continuum polarization of around 19% (Vernet et al. 2001), and the Ly α nebula associated with this object has a polarization of $16.4 \pm 4.6\%$ in its outer, eastern region (Humphrey et al. 2013b), indicating that the nebula is partly powered by the scattering of Ly α photons by HI.

Humphrey et al. (2013b) detected two continuum sources at a distance of $\sim 7''$ from the centre of the radio source. The sources were detected at the edges of the Ly α halo, one of which was found to be polarized and was also detected in H α confirming its association with this radio galaxy. They proposed that the two continuum sources were

part of a shell of gas and dust around the Ly α halo, visible because it was illuminated by the active nucleus.

2.2 TXS 0828+193

TXS 0828+193 has a large radio source (98 kpc, Carilli et al. 1997), with a total radio flux at 4.7 GHz of 22 mJy. It is found at $z=2.57$ (van Ojik 1995) and has an R-band magnitude of 20.7 (Carilli et al. 1997).

The radio structure consists of several clumps (Pentericci et al. 1999), and has a double morphology (Röttgering et al. 1994) with a jet extending from the core to the northern hotspot. The UV continuum is elongated and aligned with the axis of the radio source (Pentericci et al. 1999).

The host galaxy has a maximum stellar mass of $<3.98 \times 10^{11} M_{\odot}$ (Seymour et al. 2007). van Ojik et al. (1997) found that the blue wing of the Ly α emission profile is absorbed by neutral gas. Nesvadba et al. (2009) found CO(3-2) emission in the halo of the radio structure. This source has an intermediate continuum polarization of around 10% (Vernet et al. 2001).

Villar-Martín et al. (2002) discovered a giant halo (~ 130 kpc) of quiescent gas extending beyond the radio structures. They also detected two kinematic components in Ly α , CIV and HeII. A kinematically quiescent component (FWHM <400 km s $^{-1}$) extending across the whole object and beyond the radio structures, and a kinematically disturbed component (FWHM ~ 1200 km s $^{-1}$) inside the radio structures. While the disturbed component traces an outflow triggered by the interaction between the ambient gas and the radio structures (Humphrey et al. 2006, Humphrey et al. 2007a) found evidence of infall for the quiescent gas. Villar-Martín et al. (2002) constrained the extended gas metallicity to be close to solar.

3 OBSERVATIONS AND DATA REDUCTION

The new observations presented here were obtained using the Optical System for Imaging and low-Intermediate-Resolution Integrated Spectroscopy (OSIRIS, Cepa et al. 2000, 2003) on the 10.4 m Gran Telescopio Canarias (GTC) as part of the observing proposal 2-GTC2/11BIACMEX. The instrument was operated in long-slit spectroscopy mode with 100 kHz CCD readout mode. The two targets were observed with the R1000B grism. Long-slit spectra were obtained for TXS 0211-122 and TXS 0828+193 with total integration time of ~ 2 hours per target, split into 9 integrations of ~ 800 seconds. A $0.41''$ wide slit was used for TXS 0211-122 and a $0.8''$ wide slit was used for TXS 0828+193. The spatial pixel scale is $0.254''$ per pixel. The slit was positioned perpendicularly to the major axis of the radio and optical emission. A summary of the observations is presented in Table 1.

The data were reduced, calibrated and corrected for reddening caused by Galactic extinction using standard IRAF (Image Reduction and Analysis Facility, Tody 1993) routines.

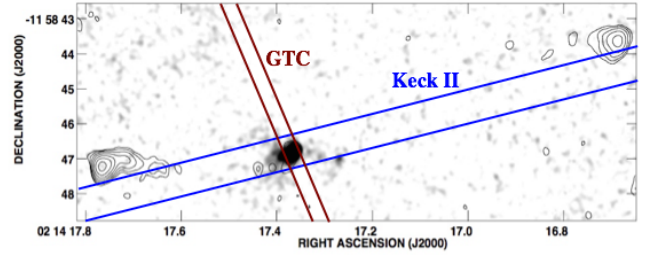


Figure 1. Radio image of the full field of TXS 0211-122 (Pentericci et al. 1999) with the positions and widths of the long slits overlotted. The long slits are much longer than the dimension of the images.

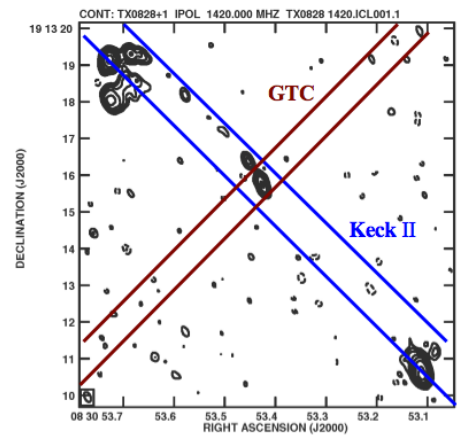


Figure 2. MERLIN³ radio image of TXS 0828+193. The positions and widths of the slits are overlotted. The long slits are much longer than the dimension of the images.

3.1 Keck II data

In addition to the new observations we made use of existing observations of TXS 0211-122 and TXS 0828+193 obtained using the Low Resolution Imaging Spectrometer (LRIS, Oke et al. 1995) at the Keck II 10 m telescope. A 300 line mm $^{-1}$ grating and a $1''$ wide slit were used, providing a dispersion of 2.4 \AA and an effective resolution of $\sim 10 \text{ \AA}$. The spectral range was $\sim 3900 - 9000 \text{ \AA}$. The spatial scale is $0.214''$ per pixel. The slit was oriented along the radio axis of the galaxy. TXS 0211-122 was observed using a position angle (PA) of 104° , and TXS 0828+193 using a PA of 44° . During the observations the seeing varied between ~ 0.5 and $1''$. For observations and data reduction details see Vernet et al. (2001). Results from this data have previously been published by Vernet et al. (2001); Villar-Martín et al. (2002, 2003); Humphrey et al. (2007a,b, 2008a).

The positions and widths of the slits are shown in Fig. 1 and 2.

3.2 Data Analysis

IRAF routines were used to measure the emission-line fluxes from simple line integrals. Kinematic information was ex-

³ MERLIN is a National Facility operated by the University of Manchester at Jodrell Bank Observatory on behalf of STFC.

Table 1. Journal of observations

Journal of observations. (1) Object name; (2) redshift; (3) date of the observations; (4) total exposure time; (5) slit position angle in degrees of North (i.e. N=0, E=90); (6) full width at half maximum of the seeing disc; (7) resolution; (8) sky transparency.

Object (1)	z (2)	Date obs. (2011) (3)	Exp. (s) (4)	PA ($^{\circ}$) (5)	Seeing ($''$) (6)	Spectral resolution (\AA) (7)	Sky transparency (8)
TXS 0211-122	2.340	30 September	7200	22.5	0.92 ± 0.02	3.1 - 4.0	Clear
TXS 0828+193	2.572	28 November	7380	- 45	1.0 ± 0.03	6.2 - 9.3	Clear

tracted from the two dimensional spectra by fitting single Gaussians to the spatial profiles of the emission lines. Gaussians were fitted at each spatial position along the slit, summing a number of spatial pixels to increase S/N. The velocity and FWHM were measured from the Gaussians fitted to the emission lines. The FWHM was corrected in quadrature for instrumental broadening. The systemic velocity was determined from the central wavelength of a Gaussian fit to the HeII emission line in the centre of the galaxy. The zero points of the spatial scales correspond to the location of the peak of the UV continuum which is assumed to be coincident with the location of the nucleus of the galaxy. This is assumed because, as already discussed by [Pentericci et al. \(2001\)](#) and [Villar-Martín et al. \(2003\)](#) the radio core of the two radio galaxies is spatially coincident with the UV continuum peak. 3σ errors were estimated using the statistical properties of the spectra.

Our main goal in this work was to study the properties of the extended gas, thus we needed to determine if the emission lines in the GTC spectra were extended. In order to do this we compared the spatial profile of the emission lines with the seeing. To determine the seeing profile in the observations the spatial profile of the seeing disc along the slit was rebuilt using a star present in the acquisition image. An aperture equal to the slit width in each observation was then used to extract the stellar flux. Due to the slit widths, the stellar profiles obtained using this method have slightly narrower FWHMs than the seeing of the observations.

3.3 Archival HST data

Images of TXS 0828+193 were obtained from the HST science archive (PI: George Miley, Proposal ID 11738). These images were taken with the Advanced Camera for Surveys (ACS) and the Wide Field Camera 3 (WFC3) of HST. TXS 0828+193 was observed on 2010 March 26th and on 2010 March 28th with the Wide Field Channel (WFC) of ACS. The WFC has a field of view of $202'' \times 202''$ and a pixel scale of $0''.049$ per pixel. To carry out these observations the filters F814W and F606W were used. The total exposure time was 10173 seconds in F814W and 10173 seconds in F606W.

TXS 0828+193 was also observed on 2010 March 10th and on 2011 May 8th with the IR Channel of the Wide Field Camera 3 (WFC3) using the filters F110W and F160W. The IR Channel has a total field of view of $123'' \times 136''$ with a pixel scale of $0.13''$. The FWHM resolution of HST/WFC3 and ACS during the observations was $0''.07 - 0''.14$. Table 2 gives details of the observations, the spectral range covered by each of the filters and the rest frame of TXS 0828+193.

4 PHOTOIONIZATION MODELS

Our photoionization model runs were performed using the multipurpose code MAPPINGS 1e ([Binette et al. 1985](#); [Ferland et al. 1997](#)). In these models it is considered that an ionizing continuum of the form $f_{\nu} \propto \nu^{\alpha}$ illuminates an isobaric, plane-parallel slab of gas. The model has several parameters: gas density of hydrogen (n_H), ionization parameter (U), spectral index of the ionizing continuum (α), and gas metallicity (Z). The ionization parameter is defined as

$$U = \frac{Q}{4\pi r^2 n_H c}, \quad (1)$$

where Q is the ionizing photon luminosity, r is the distance of the ionized cloud from the ionizing source, c is the speed of light, and n_H is the hydrogen gas density. It indicates how intense the ionizing radiation is as felt by the cloud. In the grid of photoionization calculations, U increases from 0.00005 to 0.00005×3^9 in multiplicative steps of times 3.

Photoionization by a power law of index -1.0 was used because according to the results of [Villar-Martín et al. \(1997\)](#) it is best able to reproduce the ratios observed in HzRGs. For the hydrogen density, a value of $n_H=100 \text{ cm}^{-3}$ was chosen because previous studies have found, by various lines of argument, that the extended emission line gas has very approximately this density ([McCarthy et al. 1990](#); [Villar-Martín et al. 2002, 2003](#)).

Finally, the gas metallicity takes the values $Z=0.2 Z_{\odot}$, $Z=Z_{\odot}$ and $Z=3 Z_{\odot}$, where Z_{\odot} is the solar metallicity ([Asplund et al. 2006](#)). The chemical abundances have been scaled with all metals scaled proportionally to oxygen, except nitrogen, which is scaled quadratically with oxygen ([Henry et al. 2000](#)).

Besides photoionization by the AGN, ionizing shocks may also play a role in heating the gas (e.g. [Villar-Martín et al. 1999a](#); [Tadhunter et al. 2000](#)), therefore shock and shock plus precursor models computed by [Allen et al. \(2008\)](#) using the code MAPPINGS III are also considered. In order to be consistent we chose $n_H=100 \text{ cm}^{-3}$. The models available with this hydrogen density have solar metallicities. The shock velocities are in the range $100 \text{ km s}^{-1} \leq v \leq 1000 \text{ km s}^{-1}$. [Overzier et al. \(2005\)](#) derived a magnetic field strength of $\sim 100 - 200 \mu\text{G}$ for TXS 0828+193, thus we chose $B=100 \mu\text{G}$, and the magnetic parameter $B/n^{1/2}=10 \mu\text{G cm}^{3/2}$, where n is the pre-shock number density.

Table 2. HST observations of TXS 0828+193

Journal of observations. (1) Instrument; (2) filter; (3) integration time in seconds; (4) date of the observations; (5) minimum wavelength; (6) effective wavelength; (7) maximum wavelength; (8) rest frame wavelength range; (9) main emission lines; (10) galactic extinction.

Instrument	Filter	Int. Time (s)	Date obs. (TU)	Min. λ (\AA)	Eff. λ (\AA)	Max. λ (\AA)	Rest frame (\AA)	Main emission lines	Galactic extinction
(1)	(2)	(3)	(4)	(5)	(6)	(7)	(8)	(9)	(10)
ACS	F606W	10173	2010 March 28 th	4633	5808	7180	1297.03 - 2010.08	CIII] λ 1909 HeII λ 1640 CIV λ 1549	0.085 \pm 0.01
ACS	F814W	10173	2010 March 26 th	6885		8800	1927.49 - 2463.61	CII] λ 2326 [NeIV] λ 2424	0.058 \pm 0.02
WFC3	F110W	2470	2010 March 10 th	9319	11534	13749	2608.90 - 3849.10	[OII] λ 3727 [NeV] λ 3426 MgII λ 2800	0.029 \pm 0.005
WFC3	F160W	2611	2011 May 8 th	14027.5	15369	16710.5	3927.07 - 4678.19	H γ λ 4342 [OIII] λ 4364	0.02 \pm 0.005

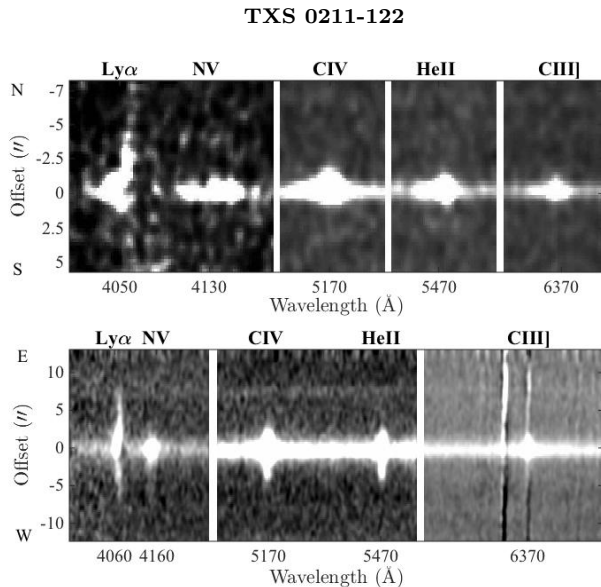


Figure 3. Top panel: Sections of the two dimensional GTC spectrum of TXS 0211-122 obtained with the slit oriented perpendicularly to the radio axis (PA=22.5°). The spectra are smoothed with a gaussian function with radius of 3 pixels to better show the emission line features. Bottom: Two dimensional Keck II spectrum of the main emission lines of TXS 0211-122, with the slit oriented along the radio axis (PA=104 °). The position of the radio core (0) is identified with the brightest continuum emission.

5 RESULTS AND ANALYSIS

5.1 TXS 0211-122

The two dimensional spectra of TXS 0211-122 are shown in Fig. 3. They show the spatial distribution of the brightest emission lines along the slits. Several emission lines show spatial asymmetry. The Ly α emission is spatially extended along both slit position angles.

The one dimensional spectra showing different regions of TXS 0211-122 from the perpendicular slit (PA=22.5°) are shown in Fig. 4. Ly α emission shows clear signs of absorp-

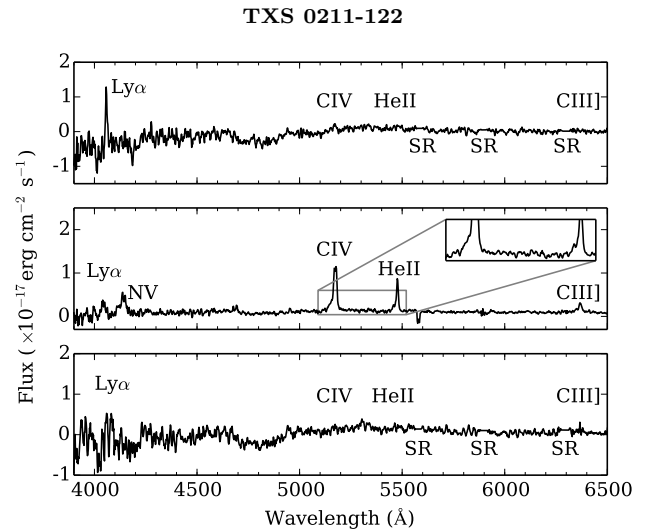


Figure 4. One dimensional spectra of different regions of TXS 0211-122 observed with the slit positioned perpendicularly to the radio axis. The top spectrum shows the region between -7'' and -1.3'', the middle figure shows the nuclear region (central 2''), and the bottom spectrum shows the region between 1.3'' and 7.6''. The name of each emission line is marking the position of the line. The spectra have been smoothed to reduce noise and they show some skyline residuals (SR).

tion. It is asymmetric, has several peaks and dips and the flux drops below the continuum level in several regions.

The CIV λ 1548.2 and CIV λ 1550.8 emission lines are blended creating a double peaked profile. In the central region there is evidence for an excess of flux in the blue wing of HeII and CIV (see Fig. 4). Humphrey et al. (2006) proposed this is the signature of an outflow triggered by jet-gas interactions.

In the left panels of Fig. 5 the spatial profiles of the emission lines and the spatial profile of the continuum are compared with the seeing profile in the perpendicular slit (PA=22.5°). The profiles have been shifted in order to make the spatial centroid coincide with that of the stellar profile. In the right panels of Fig. 5 we show the emission lines spa-

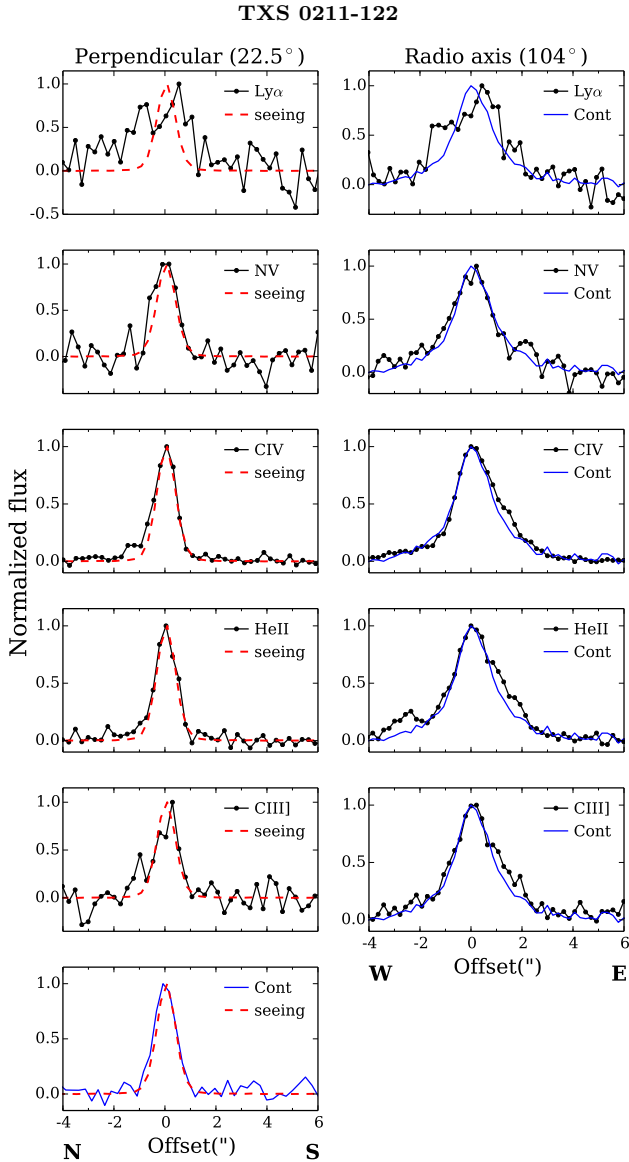


Figure 5. Normalized flux of the different emission lines (black) compared with the seeing (red) and the continuum profile (blue). In the left we show the values observed perpendicularly to the radio axis and in the right the results observed along the radio axis. Zero in the spatial direction represents the peak of the continuum emission.

tial profiles compared to the continuum profile in the observations with the slit placed along the radio axis (PA=104°).

In the GTC spectrum the spatial distribution of the Ly α , NV, CIV, HeII and CIII] emission lines is consistent with a Gaussian profile of FWHM(obs)=2.49±0.06'' for Ly α , FWHM(obs)=1.04±0.01'' for NV, FWHM(obs)=1.02±0.01'' for CIV, FWHM(obs)=1.02±0.03'' for HeII and FWHM(obs)=1.1±0.2'' for CIII]. All lines are spatially resolved compared with the seeing (FWHM=0.87±0.04''). The spatial variation of the kinematic properties of Ly α , HeII and CIV in the direction perpendicular to the radio axis (Fig.10) further confirms that the lines are spatially extended. Correcting for seeing broadening in quadrature, the

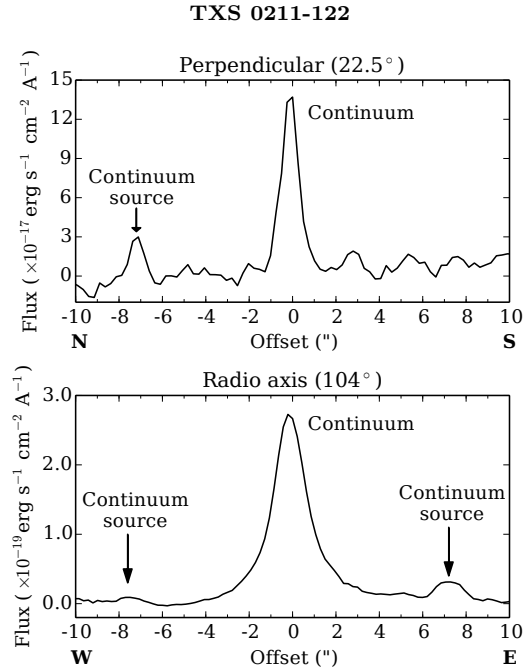


Figure 6. Continuum sources observed in TXS 0211-122. Top: continuum source observed in the perpendicular slit. Bottom: continuum sources detected in the direction of the radio axis.

intrinsic FWHM values are $2.33 \pm 0.07''$ (19.3 ± 0.6 kpc) for Ly α , $0.57 \pm 0.06''$ (4.7 ± 0.5 kpc) for NV, $0.52 \pm 0.07''$ (4.3 ± 0.6 kpc) for CIV, $0.52 \pm 0.87''$ (4.3 ± 0.7 kpc) for HeII, and $0.7 \pm 0.2''$ (6 ± 2 kpc) for CIII]. Because they are FWHM, these values should be considered lower limits to the actual extent of the emission lines. The continuum is also resolved, with FWHM=0.99±0.01''. Correcting for seeing broadening the continuum shows FWHM=0.47±0.08'' (3.9 ± 0.7 kpc). The Ly α emission shows an excess towards the North (see also Fig. 3). The excess of emission above the seeing wings shows that at $\sim 2''$ Ly α is dominated by extended emission. In the direction of the radio axis (Keck II, PA=104°) the emission lines are more extended. As van Ojik et al. (1994) and Villar-Martín et al. (2003) have already shown Ly α has a total detected extent of ~ 110 kpc. CIV and HeII are also extended, showing that the nebula is ionized and is significantly enriched in metals (Villar-Martín et al. 2003).

5.1.1 Offset UV Continuum Source

In the GTC spectrum (PA=22.5°) a faint continuum source is detected at $7.1'' \pm 0.1''$ (59 ± 1 kpc) from the centre of the galaxy (see top panel of Fig. 6). It is detected on the side to which Ly α is more extended.

The source has a FWHM of $0.8'' \pm 0.3''$ and a signal to noise ratio of 4.8. Assuming that the source is associated with the radio galaxy, the rest-frame wavelength range where the source is detected is $\sim 1900 \text{ \AA} - \sim 2300 \text{ \AA}$. No emission lines are detected from this source.

This continuum source is reminiscent of the pair of similarly offset UV continuum sources detected previously by Humphrey et al. (2013b), along PA=104°. The sources are visible in the bottom panel of Fig. 6 at $-7.3''$ and $7.4''$ from

the centre of the radio galaxy. This result will be discussed further in Section 6.

5.1.2 Line ratios and comparison with models

In order to better understand the properties and physical conditions in the large scale Ly α halo, emission line fluxes and ratios were measured from several spatial apertures, for comparison against the ionization models. The apertures are optimised to detect faint lines and low surface brightness extended emission. Table 3 and Table 4 show line ratios for GTC and Keck II data, respectively. The nuclear aperture shows a difference in line ratios between the Keck II data and GTC data but this could be due to a slight misalignment between the slits and/or to the different apertures chosen in each case.

Fig. 7 shows how the line ratios vary along the slits. The emission line ratios of this radio galaxy show strong NV and weak Ly α relative to the other emission lines (compared with typical values in HzRGs, e.g. McCarthy 1993; Humphrey et al. 2008a). The ratio between Ly α and the other emission lines presents a "U shape" along both slits. This provides evidence for a variation in Ly α absorption, with strong absorption in the central regions, and progressively less absorption at larger radii.

HzRGs showing strong Ly α absorption often show significant CIV absorption (e.g. Binette et al. 2000; Humphrey et al. 2013a). We find no evidence for CIV absorption in the form of unusually low CIV flux ratios or a U-shaped CIV line ratio curve reminiscent of Ly α . However, without higher spectral resolution (FWHM $\lesssim 10$ km s $^{-1}$) we are unable to definitively rule out the presence of CIV absorption.

Line ratios between the different emission lines are now compared to the ionization models. Diagnostic diagrams were constructed in order to visualize the comparison.

According to the diagnostic diagrams involving CIV, HeII and CIII] in Fig. 8 a photoionization model with $Z=3Z_{\odot}$ and a spatial variation in ionization parameter is able to reproduce our flux ratio measurements. However, the region from 0.8" to 1.8" can be reproduced by a photoionization model with $Z=3Z_{\odot}$ or by a photoionization model with $Z=0.2Z_{\odot}$. This illustrates the strong degeneracy between metallicity solutions when using the CIV, HeII and CIII] line ratios.

In the direction perpendicular to the radio axis NV is only detected in the centre of the galaxy. The NV strength in relation to CIV and HeII suggests high levels of chemical enrichment of the gas. The ratio NV/HeII versus NV/CIV suggests a metallicity of $Z=3Z_{\odot}$. The small variation in CIII]/HeII suggests little or no variation in C/He and, C/H.

Next, we compare the observed and model line ratios for PA=104° (along the radio axis). The diagnostic diagrams are shown in Fig. 9. In aperture -5.8" to -3.9" the degeneracy due to the use of CIV, HeII and CIII] line ratios is clearly apparent. The line ratios observed in aperture -3.9" to -1.9" lie far from the models in most of the diagrams. Both a photoionization model with $Z=0.2Z_{\odot}$ and $Z=3Z_{\odot}$ and a variation in the ionization parameter are able to reproduce our results.

The models are not able to reproduce the Ly α /HeII and Ly α /CIV line ratios. The photoionization models, shock and shock plus precursor models all predict higher Ly α /HeII ratios than those measured. The cause of this discrepancy

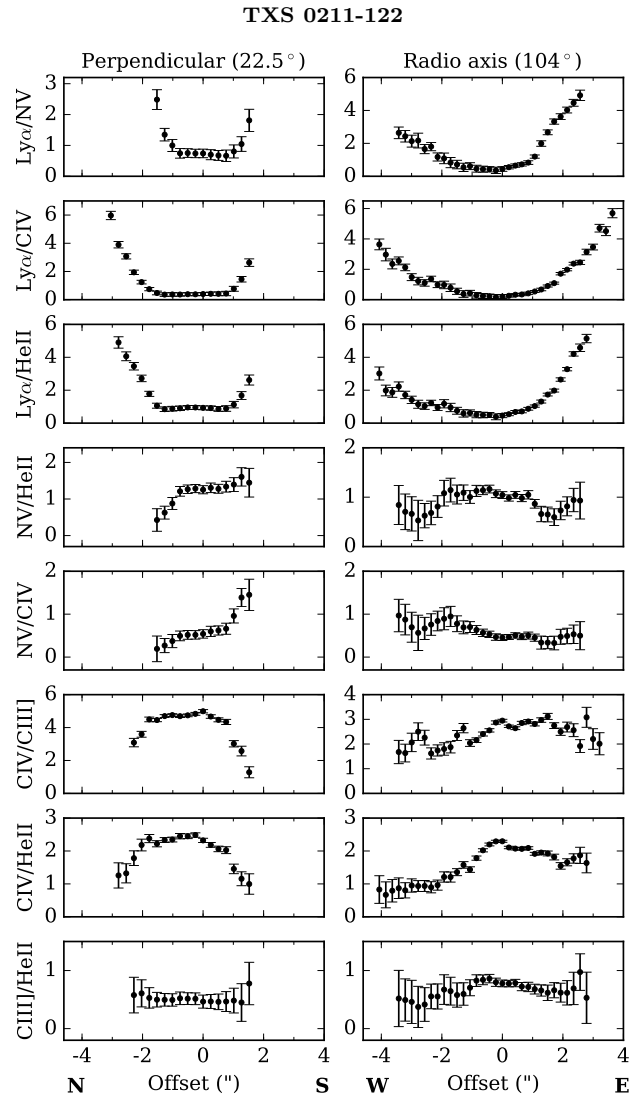


Figure 7. Ratios between the emission lines of TXS 0211-122 as a function of distance in the galaxy. In the left we have the flux ratios in the direction perpendicular to the radio axis (PA=22.5°) and in the right in the direction of the radio axis (PA=104°).

is likely to be strong absorption of Ly α by HI (and possibly dust, van Ojik et al. 1994). The diagnostic diagrams suggest supersolar metallicities, even in regions far from the nucleus. These results are in agreement with the results from Villar-Martín et al. (1999c); Vernet et al. (2001); Villar-Martín et al. (2001) who found that the metallicities of the extended emission line regions of powerful HzRGs are close to solar or supersolar. However, some HzRGs show evidence for lower metallicities (e.g. Overzier et al. 2001; Iwamuro et al. 2003).

5.1.3 Kinematics

In the left panel of Fig. 10 we show the overall velocity centroids of Ly α , HeII and CIV emission along the two long slits for TXS 0211-122. The emission lines show strong spatial variation in their velocity centroids.

The maximum difference of the Ly α emission line velocity and the systemic velocity of the galaxy observed per-

Pos. (1)	Ly α /HeII (2)	Ly α /CIV (3)	Ly α /NV (4)	CIV/HeII (5)	CIV/CIII] (6)	NV/HeII (7)	NV/CIV (8)
-3.3'' : -1.8''	5.0 \pm 0.3	-	-	-	-	-	-
-1.8'' : -0.8''	2.9 \pm 0.2	1.5 \pm 0.2	-	2 \pm 0.2	3.1 \pm 0.2	-	-
-0.8'' : 0.8''	0.8 \pm 0.1	0.34 \pm 0.1	0.5 \pm 0.1	2.36 \pm 0.06	4.51 \pm 0.08	1.56 \pm 0.09	0.66 \pm 0.08
0.8'' : 1.8''	2.5 \pm 0.3	1.6 \pm 0.3	-	1.5 \pm 0.3	1.9 \pm 0.3	-	-

Table 3. Emission line ratios from several apertures in the TXS 0211-122 spectrum observed in the direction perpendicular to the radio axis (PA=22.5°). Columns are as follows: (1) position of the aperture along the slit in arcseconds; (2) the Ly α /HeII ratio; (3) the Ly α /CIV ratio; (4) the Ly α /NV ratio; (5) the CIV/HeII ratio; (6) the CIV/CIII] ratio; (7) the NV/HeII ratio; (8) the NV/CIV ratio.

Pos. (1)	Ly α /HeII (2)	Ly α /CIV (3)	Ly α /NV (4)	CIV/HeII (5)	CIV/CIII] (6)	NV/HeII (7)	NV/CIV (8)
-5.8'' : -3.9''	5.4 \pm 0.3	3.6 \pm 0.3	-	1.5 \pm 0.4	1.7 \pm 0.4	-	-
-3.9'' : -1.9''	1.3 \pm 0.1	1.4 \pm 0.1	1.4 \pm 0.1	1.0 \pm 0.1	3.3 \pm 0.2	0.9 \pm 0.2	1.0 \pm 0.2
-1.9'' : 1.3''	0.65 \pm 0.05	0.33 \pm 0.04	0.67 \pm 0.04	1.94 \pm 0.03	3.43 \pm 0.05	0.96 \pm 0.05	0.49 \pm 0.04
1.3'' : 4.1''	4.4 \pm 0.1	2.52 \pm 0.07	4.58 \pm 0.09	1.8 \pm 0.1	2.8 \pm 0.12	1.0 \pm 0.2	0.5 \pm 0.2

Table 4. Emission line ratio measurements from the TXS 0211-122 spectrum, observed along the radio axis (PA=104°). Columns are as in 3.

pendicularly to the radio axis (PA=22.5°) is $\sim 1400 \text{ km s}^{-1}$. The maximum velocity shift of HeII and CIV across the nebula are $\sim 130 \text{ km s}^{-1}$ and $\sim 150 \text{ km s}^{-1}$, respectively. In the direction perpendicular to the radio axis HeII and CIV show similar velocity curves to each other, but both differ greatly from the velocity curve of Ly α , suggesting that the measured kinematics of Ly α emission are strongly affected by HI absorption and/or scattering.

In the direction of the radio axis (PA=104°) the maximum difference between Ly α velocity and the systemic velocity is $\sim 1000 \text{ km s}^{-1}$. HeII shows a maximum velocity shift of $\sim 230 \text{ km s}^{-1}$ and CIV has a maximum velocity shift of $\sim 600 \text{ km s}^{-1}$. In this direction HeII shows a rather constant velocity curve. The velocity curve of Ly α shows a large range in velocity. Once again this could be due to HI absorption or scattering. The velocity curve of CIV also differs from the velocity curve of HeII, and CIV appears to be blueshifted relative to HeII. This result is further explored later in this section.

The right panel of Fig. 10 shows how the FWHM of Ly α , HeII and CIV vary along the two slits. In the direction perpendicular to the radio axis there is a sudden jump in the FWHM and velocity curve of Ly α at -1.5''. This jump is not seen in the other UV lines, suggesting a change in the impact of absorption or resonant scattering on Ly α .

In the direction of the radio axis (PA=104°) Ly α shows several changes in the FWHM. Villar-Martín et al. (2003) found narrow and broad components in the Ly α emission of this radio source. The differences in the FWHM(Ly α) observed in Fig. 10 may be due to the different components. In regions where the broad component is affecting more the width of the line broad lines are produced, and in regions

where the narrow component dominates the FWHMs are lower.

The velocity curve of HeII displays perturbed kinematics⁴ (FWHM < 1000 km s⁻¹) along both PAs. The observed FWHM are higher than what we would expect from gravitational motions (e.g. Villar-Martín et al. 2002). In addition, Ly α and CIV show high FWHM in both PAs, suggesting that there are highly perturbed motions along both axes.

5.1.4 Correlations between kinematics and line ratios

Looking at the results obtained for the Keck II data (PA=104°) and comparing the figure of CIV/HeII (Fig. 7) and the velocity of CIV (Fig. 10) it can be seen that the lowest values of CIV/HeII have the highest blueshift. This result is consistent with the presence of ionized gas outflows along the radio axis, with a relatively lower ionization state, as has been found in a number of powerful radio galaxies at low to high redshifts (e.g. Villar-Martín et al. 1999a; Humphrey et al. 2006).

In order to investigate possible correlations between the CIV/HeII ratio and the velocities of the different emission lines the Spearman (1904) rank correlation coefficient, ρ , was calculated.

The results are presented in Fig. 11. There is a strong correlation ($\rho=0.932$) between CIV's velocity and the ratio CIV/HeII in the direction of the radio axis. The figure also

⁴ In this work highly perturbed emission refers to emission lines with FWHM $\geq 1000 \text{ km s}^{-1}$ and perturbed emission refers to gas with FWHM $\leq 1000 \text{ km s}^{-1}$.

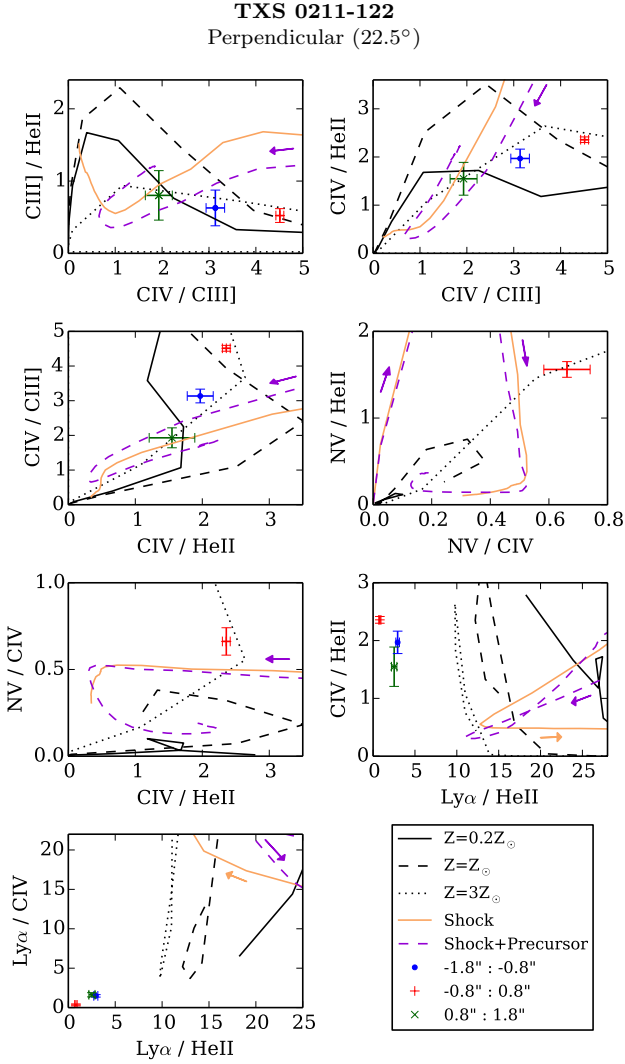


Figure 8. Diagnostic diagrams involving the $\text{Ly}\alpha$, NV, HeII, CIV and CIII] emission lines. The black lines represent sequences of photoionization models for three different metallicities. U varies along each metallicity line. Shock models by Allen et al. (2008) are also shown. Orange solid lines denote the predictions of pure shock models, and violet-dotted lines denote the prediction of shock plus precursor models. The arrows indicate the direction of increasing shock velocity.

shows a correlation ($\rho=0.620$) between HeII’s velocity and CIV/HeII. The significance of the values 0.932 and 0.620 was tested by comparing them to critical values for Spearman’s rank correlation coefficient. Both correlations are significant at a confidence level of more than 99%.

In the direction perpendicular to the radio axis no correlation is apparent, suggesting that the ionized outflowing gas is preferentially situated along the radio axis.

5.2 TXS 0828+193

The two dimensional spectra of TXS 0828+193 are shown in Fig. 12. $\text{Ly}\alpha$ is the brightest and most extended emission line along both PAs.

One dimensional spectra showing different regions of TXS 0828+193 observed with the slit positioned perpendic-

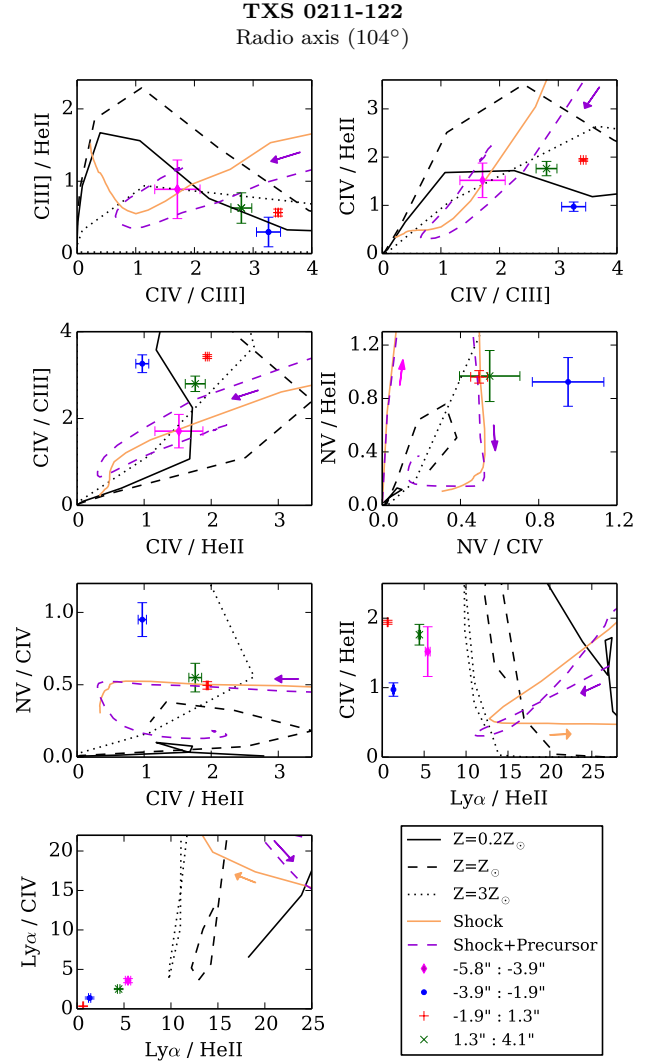


Figure 9. Flux ratios of TXS 0211-122 observed with the slit placed along the radio axis plotted on diagnostic diagrams involving $\text{Ly}\alpha$, NV, CIV, HeII and CIII]. The diagrams are the same as in Fig. 8.

ularly to the radio axis are shown in Fig. 13. An excess of emission in the blue wing of $\text{Ly}\alpha$ is seen in the middle and bottom panels of Fig. 13.

In Fig. 14 we show the spatial profiles of the different emission lines and the spatial profile of the continuum for both PAs. For the perpendicular slit we also show the seeing ($\text{FWHM}=0.93\pm0.04''$). In the GTC spectrum ($\text{PA}=-45^\circ$) $\text{Ly}\alpha$ has an extent of $6.9''$ (~ 56 kpc), much less than the ~ 130 kpc extent *along* the radio axis measured by Villar-Martín et al. (2002).

The spatial distribution of the $\text{Ly}\alpha$, CIV, HeII and CIII] emission lines is consistent with a Gaussian profile of $\text{FWHM}(\text{obs})=1.62\pm0.02''$ for $\text{Ly}\alpha$, $\text{FWHM}(\text{obs})=1.21\pm0.01''$ for CIV, $\text{FWHM}(\text{obs})=1.16\pm0.03''$ for HeII and $\text{FWHM}(\text{obs})=1.33\pm0.01''$ for CIII]. Correcting for seeing broadening in quadrature, the intrinsic FWHM values are $1.33\pm0.04''$ (10.8 ± 0.3 kpc) for $\text{Ly}\alpha$, $0.77\pm0.05''$ (6.3 ± 0.4 kpc) for CIV, $0.69\pm0.07''$ (5.6 ± 0.6 kpc) for HeII, and $0.95\pm0.04''$ (7.7 ± 0.3 kpc) for CIII]. NV is consistent with

TXS 0211-122

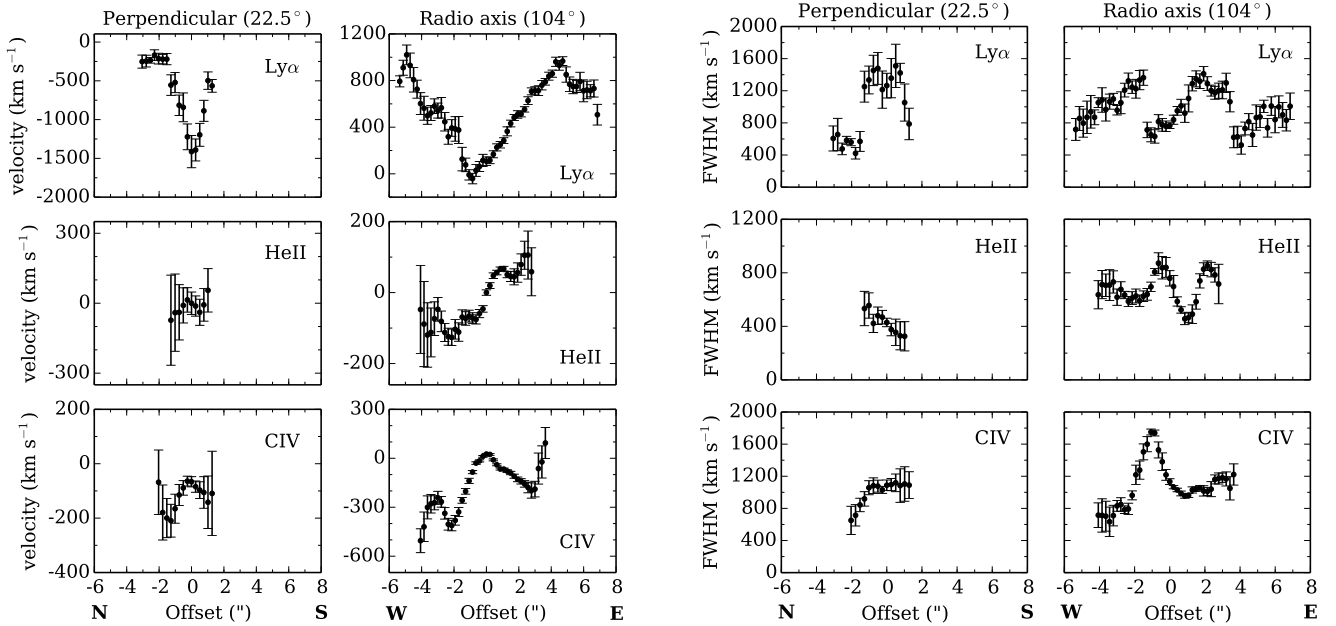


Figure 10. Left: Velocity profiles of Ly α (top), HeII (middle) and CIV (bottom). Right: FWHM of Ly α , HeII and CIV. The figures in the left represent the variation in the direction perpendicular to the radio axis, while the figures in the right represent the variation along the radio axis.

the seeing, we determine an upper limit of $0.97''$ for the FWHM. After correcting for seeing broadening the intrinsic FWHM is $\sim 0.27''$ (2.2 kpc). The continuum is resolved, with an intrinsic FWHM of $1.24 \pm 0.08''$ (10.1 ± 0.7 kpc). It is asymmetric and shows stronger emission towards the NW. In this source, all the emission lines (except NV) are spatially extended in the direction perpendicular to the radio axis. This is further supported by the fact that the kinematic properties of Ly α , CIV and HeII vary along the slit (Fig. 18).

The emission lines are more extended in the direction of the radio axis, as is also the case in TXS 0211-122.

5.2.1 Line ratios and comparison with models

Fig. 15 shows how the different emission line ratios vary along the slit. The emission line ratios in TXS 0828+193 are typical of HzRGs (e.g. McCarthy 1993; Humphrey et al. 2008a). In the direction perpendicular to the radio axis, (Fig. 15 left panels), the emission line ratios Ly α /HeII and Ly α /CIV show a peak around $\sim 2''$. Another local maximum is seen for the same line ratios at $\sim 2''$. This may suggest that Ly α emission is enhanced in these regions. However, it is not immediately clear whether this is due to enhanced Ly α or lower fluxes for the other lines. In the direction of the radio axis (Fig. 15 right) Ly α /CIV, Ly α /HeII and CIII]/HeII show a local maximum at $\sim 2''$, but this time with only two corresponding features at $\sim 2''$ (CIV/CIII] and CIV/HeII).

In order to understand the physical conditions and properties of the extended emission line regions, a comparison is made between the results of our observations and photoionization and shock models. For this purpose, several

apertures were extracted along the slits. Table 5 shows the different apertures and the flux ratios for the different emission lines in the direction perpendicular to the radio axis (PA= -45°).

To help distinguish between ionization mechanisms in the gas line-ratio diagrams were used. The models are the same as used for TXS 0211-122. In Fig. 16 diagnostic diagrams showing photoionization and shock models for the slit perpendicular to the radio axis are shown. NV is consistent with the seeing thus we did not include it in the diagrams.

In Table 6 it can be seen that in the outer regions of the nebula Ly α emission is very bright in comparison to HeII, CIV and CIII]. The variation in the ratio CIV/CIII] suggests that the state of ionization of the gas is not constant across the nebula. The ratio CIV/HeII suggests an increase in the ionization state of the gas, from NE ($\sim 3.6''$) to SW ($\sim 3.6''$). This result is in agreement with results from Humphrey et al. (2007b).

It is apparent from Fig. 16 that a photoionization model with $Z=3Z_\odot$ is able to reproduce the ratios for the region $-2.5''$ to $-1.5''$ in some diagrams. However the ratios are also reproduced by shock and shock plus precursor models. Due to the low Ly α /HeII ratio we observe the models are not able to reproduce our results. The detection of strong HeII emission strongly disfavours photoionization by young stars and resonant scattering as main powering mechanisms.

In Fig. 17 diagrams showing photoionization and shock models for the slit along the radio axis are presented. The diagram of NV/HeII versus NV/CIV suggests that the gas metallicity is high. Photoionization models with metallicities between Z_\odot and $3Z_\odot$ give the best reproduction of the results, however, due to the overlapping between the photoionization and the shock models we cannot rule out the

Pos. (1)	Ly α /HeII (2)	Ly α /CIV (3)	Ly α /CIII] (4)	CIV/HeII (5)	CIV/CIII] (6)
-4.3'' : -2.5''	2.3 \pm 0.3	3.7 \pm 0.4	-	0.6 \pm 0.4	
-2.5'' : -1.5''	2.7 \pm 0.3	2.6 \pm 0.2	3.0 \pm 0.2	1.0 \pm 0.2	1.14 \pm 0.2
-1.5'' : 1''	7.61 \pm 0.03	4.77 \pm 0.02	14.7 \pm 0.05	1.60 \pm 0.03	3.07 \pm 0.05
1'' : 2''	-	24.6 \pm 0.3	36.7 \pm 0.3	-	1.5 \pm 0.4

Table 5. Emission line ratio measurements from the TXS 0828+193 spectrum, observed perpendicularly to the radio axis (PA= -45°). Columns are as follows: (1) position of the aperture along the slit in arcseconds; (2) the Ly α /HeII ratio; (3) the Ly α /CIV ratio; (4) the Ly α /CIII] ratio; (5) the CIV/HeII ratio; (6) the CIV/CIII] ratio.

Pos. (1)	Ly α /HeII (2)	Ly α /CIV (3)	Ly α /CIII] (4)	CIV/HeII (5)	CIV/CIII] (6)	NV/HeII (7)	NV /CIV (8)
-3.6'' : -1.3''	19.39 \pm 0.08	8.94 \pm 0.04	16.33 \pm 0.06	2.2 \pm 0.1	1.83 \pm 0.07	0.6 \pm 0.2	0.3 \pm 0.2
-1.3'' : 0.9''	10.85 \pm 0.01	5.90 \pm 0.01	19.91 \pm 0.02	1.84 \pm 0.01	3.37 \pm 0.02	0.56 \pm 0.04	0.30 \pm 0.04
0.9'' : 2.8''	8.3 \pm 0.03	5.22 \pm 0.02	20.92 \pm 0.06	1.60 \pm 0.04	4.01 \pm 0.06	0.3 \pm 0.2	0.3 \pm 0.2
2.8'' : 3.6''	6.5 \pm 0.2	5.0 \pm 0.2	-	1.3 \pm 0.2	-	-	-

Table 6. Emission line ratio measurements from the TXS 0828+193 spectrum, observed along the radio axis (PA= 44°). Columns are as in Table 5.

possibility that both mechanisms are ionizing the gas. This is in agreement with the results of [Humphrey et al. \(2008a\)](#) who showed that AGN photoionization is the main ionization mechanism in radio galaxies but shocks also make a small contribution to the ionization of the gas.

5.2.2 Kinematics

The velocity curves of Ly α , CIV and HeII are shown in the left panel of Fig. 18. Perpendicularly to the radio axis HeII shows a near systemic velocity curve (within the error bars). In the same region CIV also presents near systemic velocities. The CIV velocity curve resembles that of Ly α .

In the centre of the galaxy Ly α emission is redshifted ($v_{Ly\alpha} \sim 340 \text{ km s}^{-1}$) relatively to HeII. The modulus of the maximum difference in radial velocity of HeII is $\Delta v(\text{HeII}) \sim 220 \text{ km s}^{-1}$, for CIV the maximum difference in radial velocity $\Delta v(\text{CIV}) \sim 310 \text{ km s}^{-1}$.

There is a velocity shift ($\sim 340 \text{ km s}^{-1}$ for PA= -45° , and $\sim 220 \text{ km s}^{-1}$ for PA= 44°) between Ly α and HeII. There are at least two possible reasons for this. First, Ly α and HeII may originate in gas from different locations, and thus different kinematic properties, in the overall nebulosity. Secondly, Ly α can be shifted from other lines as a consequence of partial absorption of the Ly α emission by HI (e.g. [Röttgering et al. 1995](#); [van Ojik et al. 1997](#)). In this case, Ly α must be absorbed in the central regions because Ly α /HeII and Ly α /CIV are well below the photoionization model predictions.

In the direction perpendicular to the radio axis (PA= -45°) Ly α emission (Fig. 18) from the central regions show an approximately constant redshifted velocity relatively to

HeII. In this direction there are some changes in the velocity pattern of Ly α at $\sim 2''$ and $\sim 2''$.

In the direction of the radio axis (PA= 44°) we see that HeII and CIV show similar velocity curves. At $\sim 2''$ and $\sim 2''$ CIV and HeII show local maxima in their velocity curves.

The right panel of Fig. 18 shows the FWHM of the emission lines as a function of distance from the nucleus. In the direction perpendicular to the radio axis (PA= -45°) the emission lines show large FWHMs ($> 1000 \text{ km s}^{-1}$).

5.2.3 HST observations

Fig. 19 shows the HST images of TXS 0828+193. As already noted by [Pentericci et al. \(1999\)](#) using a relatively shallower WFPC2 image, in the central $\sim 2''$ of the galaxy the rest-frame UV and optical emission shows a triangular morphology and is closely aligned with the position angle of the radio source, with a number of relatively bright and compact clumps embedded within a diffuse low surface brightness component.

The new HST images reveal additional, faint morphological features in TXS 0828+193. Thanks to the greater depth of our images, the diffuse UV emission on the NE side of the galaxy, also detected in the WFPC2 image of [Pentericci et al. \(1999\)](#), is revealed to have a double-shell/loop morphology. This feature is detected in all 4 of the HST images, and is reminiscent of the super-bubble morphology seen in HST images of MRC 0406-244 ([Rush et al. 1997](#); [Pentericci et al. 2001](#); [Taniguchi et al. 2001](#); [Humphrey et al. 2009](#); [Hatch et al. 2013](#)).

In the F160W image, the morphology in the central

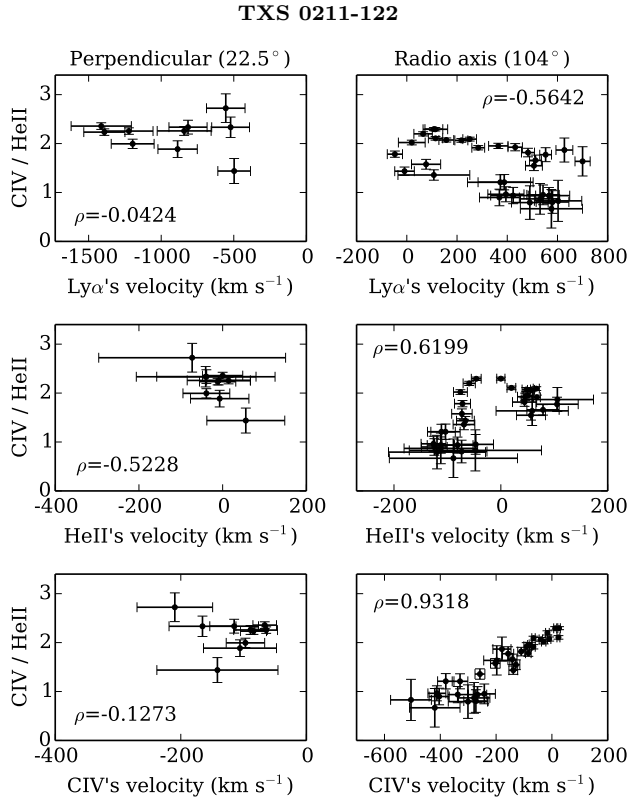


Figure 11. Variation of CIV/HeII ratio with the velocity of different emission lines. The top left panel shows the ratio CIV/HeII as a function of the velocity of Ly α in the perpendicular slit, the top right panel shows the variation of CIV/HeII as a function of the velocity of Ly α along the radio axis, the middle left panel shows the variation of CIV/HeII as a function of the velocity of HeII in the perpendicular slit, the middle right panel shows the variation of CIV/HeII as a function of the velocity of HeII in the slit placed along the radio axis, the bottom left figure shows how the CIV/HeII varies with the velocity of CIV in the perpendicular slit and the bottom right figure shows how the CIV/HeII varies with the velocity of CIV along the radio axis. ρ represents the Spearman's rank correlation coefficient.

$\sim 2''$ of the galaxy shows 6 relatively compact sources with an X-shaped distribution about the central source.

6 DISCUSSION

6.1 Outflows

Perturbed/extreme kinematics are known to be present along the radio axis of several HzRGs (e.g. [Tadhunter 1991](#); [McCarthy et al. 1996](#); [Villar-Martín et al. 1999b](#)), including TXS 0211-122 and TXS 0828+193 ([Villar-Martín et al. 2002](#); [Humphrey et al. 2006](#)). In the case of TXS 0211-122, we find further evidence for this in the form of an anticorrelation between the CIV/HeII flux ratio and magnitude of the blueshift of CIV and HeII from the systemic velocity, but only along the radio axis. No such (anti)correlation is seen along the perpendicular slit, suggesting that the ionized outflow is not galaxy-wide, and is located preferentially along the radio axis. Moreover, the FWHM of the HeII emission along the perpendicular slit is consistent with gravitational

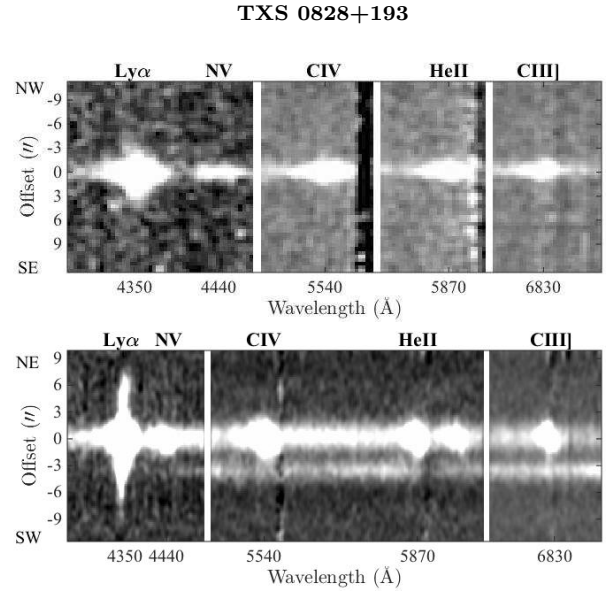


Figure 12. Top: 2D spectrum of the main emission lines for TXS 0828+193, with the slit oriented perpendicularly to the radio axis. Bottom: 2D spectrum of the main emission lines for TXS 0828+193, with the slit oriented in the direction of the radio axis. The zero in the spatial direction corresponds to the peak of the continuum emission.

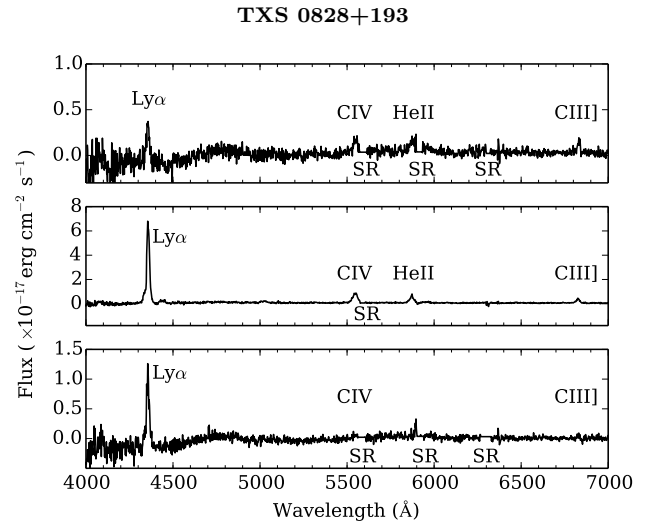


Figure 13. One dimensional spectra of different regions of TXS 0828+193 observed with the slit oriented perpendicularly to the radio axis. The top spectrum shows the region between $-4.3''$ and $-1.3''$, the spectrum in the middle shows the nuclear region (central $2''$) and the bottom spectrum shows the region between $1.3''$ and $4.6''$. Ly α , NV, CIV, HeII and CIII] positions are indicated in the spectra. NV is only detected in the central region. There are some skyline residuals (SR) affecting the emission lines. CIV emission line is affected by the 5577 \AA (OI) skyline, HeII is affected by a skyline at 5889 \AA (Na D) and CIII] is affected by a skyline at $\sim 6828 \text{ \AA}$ (OH).

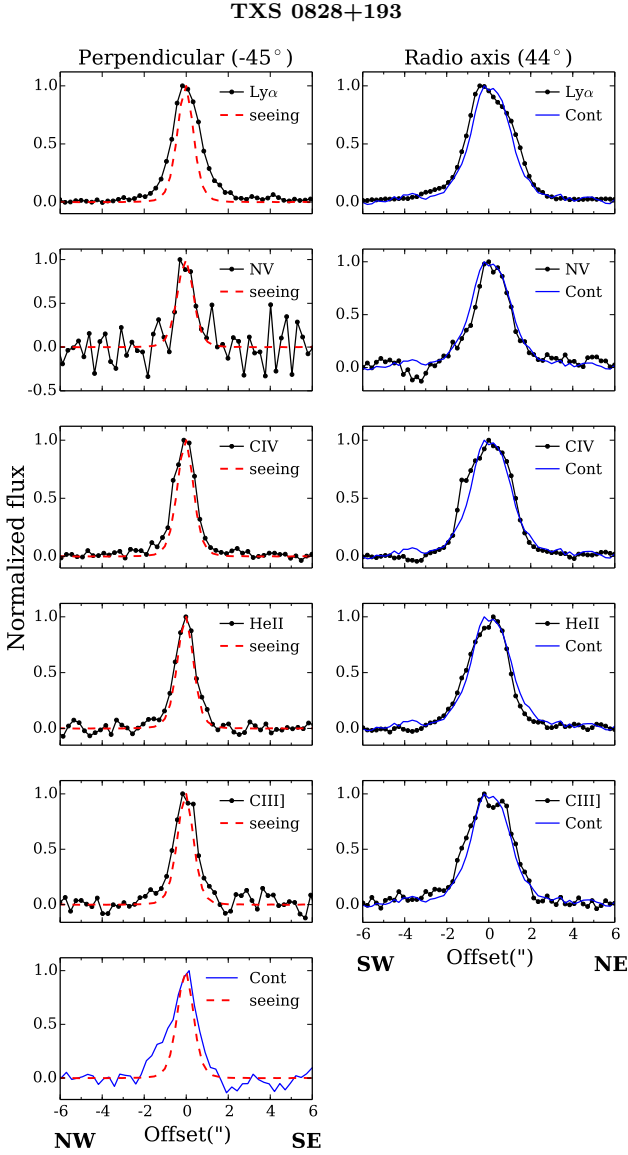


Figure 14. Normalized flux of the different emission lines (black) compared with the seeing (red) and the continuum profile (blue). In the left we have the values observed perpendicularly to the radio axis and in the right the normalized flux along the radio axis. Zero in the spatial direction represents the peak of the continuum emission.

gas kinematics ($<600 \text{ km s}^{-1}$). These results are consistent with a scenario in which the radio structures are disturbing the gas kinematics along the radio axis (e.g. Best et al. 1998; Villar-Martín et al. 1999a; Christensen et al. 2006).

In the case of TXS 0828+193, the long-slit observations show that Ly α , CIV, and HeII are relatively broad along both slit PAs. The large FWHM seen in the direction perpendicular to the radio axis is evidence that the disturbed emission line kinematics are not confined to the radio axis, with relatively broad Ly α (FWHM $>1000 \text{ km s}^{-1}$) being detected out to a radial distance of $\sim 30 \text{ kpc}$ from the nucleus. In this galaxy there seems to be an enhancement in the emission of several lines and a change in the velocity pattern at $\pm 2''$ from the nucleus, suggesting the presence of a

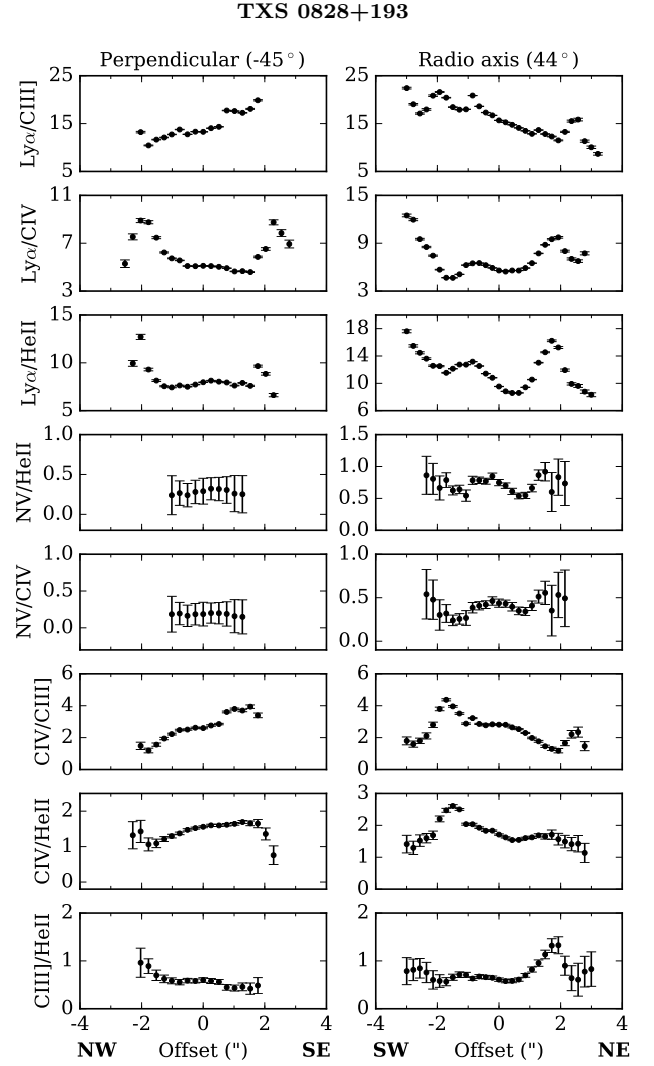


Figure 15. Ratios between the emission lines in TXS 0828+193 as a function of distance in the galaxy. In the left are shown the flux ratios in the direction perpendicular to the radio axis (PA= -45°) and in the right in the direction of the radio axis (PA= 44°).

mechanism operating at $r \sim 2''$ that is disturbing the gas and altering its excitation properties.

We argue that the above results from TXS 0828+193 can be naturally explained by a scenario consisting of an expanding bubble of gas with a radius of $\sim 16 \text{ kpc}$ ($\sim 2''$, see Fig. 20), inside which the most kinematically perturbed gas is located, and outside of which the gas kinematics are less extreme. At the edge of the bubble, one might expect there to be a shock-ionized shell of interstellar medium that has been swept up as the outflow progresses through the galaxy, although the enhancement in local gas density may also alter the ionization conditions there independently of the ionization mechanism. Interestingly, the HST images (Fig. 19) reveal an apparent bubble or loop structure located at $\sim 1.4''$ (11 kpc) to the NE along the radio axis, which we suggest may be part of this bubble.

Based on timescale arguments, we find it plausible that the expanding bubble and radio-loud activity were triggered simultaneously. In the case of the radio source, we assume

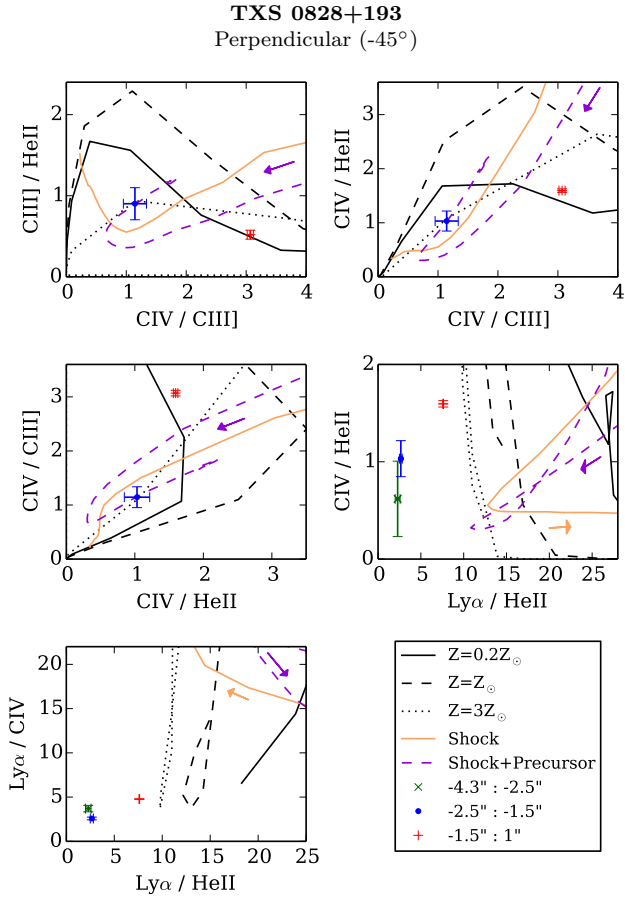


Figure 16. Flux ratios of TXS 0828+193 observed with the slit oriented perpendicularly to the radio axis plotted on diagnostic diagrams involving $\text{Ly}\alpha$, CIV, HeII and CIII]. The black lines represent sequences of photoionization models for constant metallicities. U varies along each metallicity line. Shock models by Allen et al. (2008) are also shown. Orange solid lines denote the predictions of pure shock models, and violet-dotted lines denote the prediction of shock plus precursor models. The arrows indicate the direction of increasing velocity.

an average speed of hotspot advance of $\sim 0.1c$ (e.g. Carilli et al. 1991; Liu et al. 1992; Best et al. 1995; Arshakian & Longair 2000). For a hotspot to core radius of ~ 50 kpc, we thus obtain an approximate age of $\sim 2 \times 10^7$ years.

For the expanding bubble, we assume an expansion velocity of $\sim 1000 \text{ km s}^{-1}$ (e.g. Bland & Tully 1988; Heckman 2003). Taken together with its radius of ~ 16 kpc, this gives an age of $\sim 2 \times 10^7$ years. Despite the calculated ages being rather approximate, their similarity shows that both phenomena could plausibly have been triggered at (or near) the same point in time, presumably by the AGN activity (for the jets) and feedback activity (for the bubble). A possible alternative means to explain their apparently simultaneous triggering is through a merger event, during which gas is driven into the nuclear regions of the host galaxy to trigger a massive starburst and a resultant galaxy-wide super wind, in addition to triggering radio-loud AGN activity.

Interestingly, from its velocity curve along the perpendicular slit (Fig. 18) we find that $\text{Ly}\alpha$ is almost always redshifted in relation to the systemic velocity. Taking this result at face value (ignoring line transfer effects), one might con-

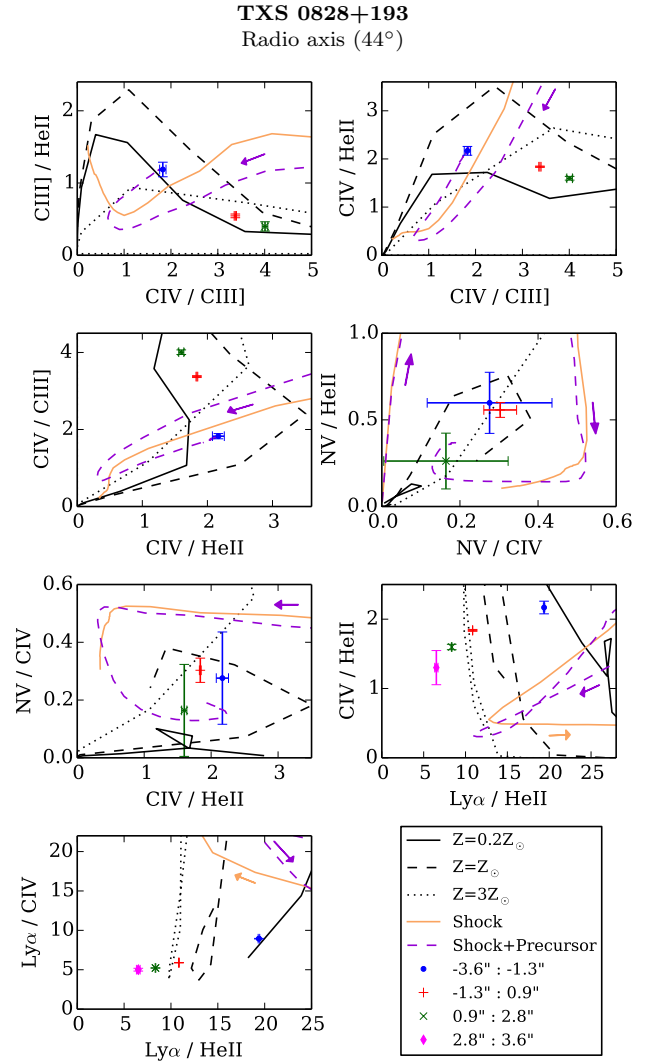


Figure 17. Flux ratios observed with the slit placed along the radio axis plotted on diagnostic diagrams involving $\text{Ly}\alpha$, NV, CIV, HeII and CIII]. The models are the same as in Figure 16.

clude that the extended $\text{Ly}\alpha$ emitting gas is infalling towards the centre of the host galaxy (e.g. Humphrey et al. 2007a, 2013a). However, the transfer of $\text{Ly}\alpha$ photons through an outflowing neutral medium may also result in the $\text{Ly}\alpha$ profile being shifted to the red (e.g. Dijkstra et al. 2006). As such, this result cannot be unambiguously interpreted.

6.2 Offset continuum sources in TXS 0211-122

Using the same Keck II long slit spectrum of TXS 0211-122 (PA=104°), Humphrey et al. (2013b) detected a pair of diametrically opposed UV continuum sources positioned ~ 60 kpc either side of the radio galaxy, at the extreme outer edge of the $\text{Ly}\alpha$ emission halo. The brighter of the two UV continuum sources was found to be linearly polarized, implying illumination by the central AGN and the presence of dust. Its detection in $\text{H}\alpha$ confirmed its similar redshift to the radio galaxy. Humphrey et al. (2013b) proposed to have detected in emission (for the first time) a giant shell of gas of the type that is thought to be responsible for the giant HI and

TXS 0828+193

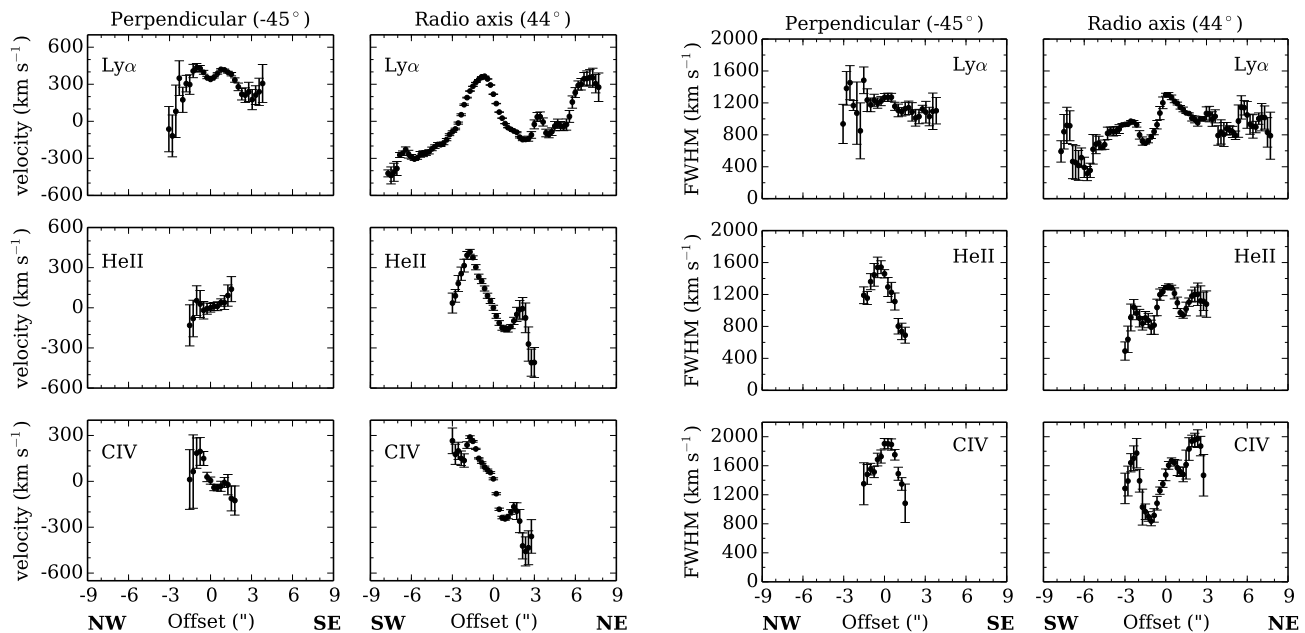


Figure 18. Left: Ly α (top), HeII (middle) and CIV (bottom) velocity profiles for TXS 0828+193. Right: FWHM for Ly α , HeII and CIV. The figures in the left represent the variation in the direction perpendicular to the radio axis, while the figures in the right represent the variation along the radio axis.

CIV absorbers detected in many HzRGs (e.g. van Ojik et al. 1997).

Our detection of a further UV continuum source, also located at ~ 60 kpc from the AGN and along a very different PA, corroborates the result of Humphrey et al. (2013b) and provides further information about the nature of this structure(s). The detection of three (compared to two) equidistant offset continuum sources now makes it even more improbable that these are merely fortuitously positioned companion galaxies. If our two slits are intersecting a single continuous structure, then it would need to cover an angle of at least 180° , and be approximately circular/semi-circular. Interestingly, our GTC spectrum shows the Ly α emission to be brightest/more extended on the side of the galaxy where the offset UV continuum source is positioned, which suggests the presence or enhancement of extended Ly α may be closely related to the offset continuum source (or vice versa). Our favoured interpretation is that this is a large-scale shell of gas and dust, produced by a powerful feedback event in the host galaxy of the HzRG, similar to the interpretation of Humphrey et al. (2013b).

A potential alternative explanation is that we may have detected the observational manifestation of an accretion shock, produced during the infall of cold gas into the host galaxy of the HzRG (e.g. Barkana & Loeb 2003; Barkana 2004; Humphrey et al. 2008b). In this scenario, infalling gas would be shocked and ionized upon reaching the virial radius, with the density of gas experiencing a local enhancement there. Unfortunately, the radius at which this effect would occur is not well constrained, but is not incompatible with the 60 kpc offsets measured for the UV continuum sources we observe (see also Humphrey et al. 2013b). However, the apparent presence of dust in at least one of the

offset UV sources would seem to disfavour an external origin.

7 CONCLUSIONS

Using long-slit spectroscopy from the 10.4 m GTC and the 10 m Keck II telescopes, we have studied the kinematics and ionization properties of the extended emission line nebulae associated with two HzRGs, TXS 0211-122 and TXS 0828+193. We have also presented previously unpublished HST images of TXS 0828+193.

In addition to the large spatial extent of Ly α emission along the radio axis reported by previous works (Villar-Martín et al. 2002, 2003), we find that both radio galaxies also show spatially very extended Ly α emission in the direction perpendicular to the radio axis. In the case of TXS 0211-122, the flux and velocity profiles of Ly α are strongly affected by HI absorption/scattering. Moreover, we find evidence for outflowing gas along the radio axis which may be the result of jet-gas interactions, in agreement with previous studies. In contrast, in our slit placed perpendicularly to the radio axis, we find less perturbed gas kinematics, which suggests outflows of ionized gas in this object are focused along the radio jet axis, rather than being galaxy-wide. We also find evidence for a large-scale UV-emitting arc or shell-like feature circumscribing the radio galaxy and the Ly α halo, possibly resulting from feedback activity.

For TXS 0828+193, extended Ly α emission (~ 56 kpc) is detected in the direction perpendicular to the radio axis, in addition to the previously reported large extent along the radio axis (130 kpc, Villar-Martín et al. 2002). Along both slit position angles we find evidence for gas with highly

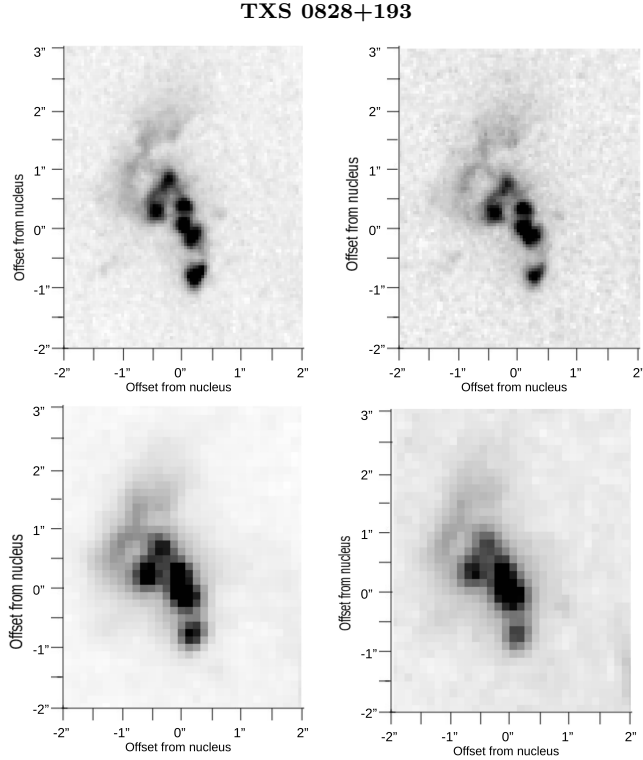


Figure 19. HST observations of TXS 0828+193 using different filters. Top left: F606W image. Top right: F814W image. Bottom left: F110W image. Bottom right: F160W image.

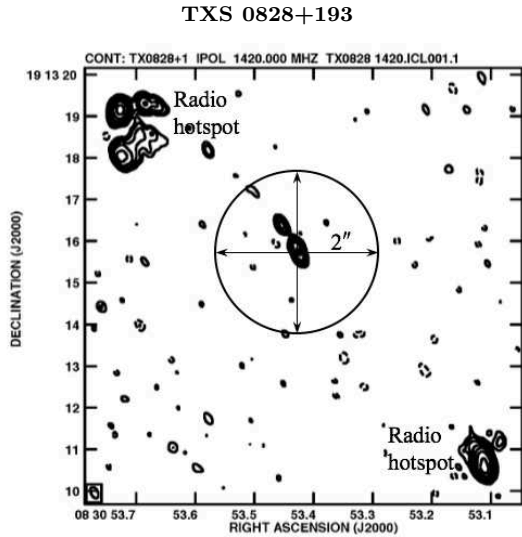


Figure 20. Expanding bubble scheme overplotted in the image of the full field of TXS 0828+193.

perturbed kinematics, which we argue is part of a roughly spherical, expanding bubble or shell of gas powered by feedback activity in the central regions of the radio galaxy. Our results suggest there is a diversity in the spatial distribution of ionized outflows in powerful radio galaxies at $z \sim 2.5$.

ACKNOWLEDGMENTS

We would like to thank Laura Pentericci for allowing us to reproduce the radio/optical image of TXS 0211-122. We thank Bjorn Emonts for the useful comments that helped improve this work. We also thank Bob Fosbury, Andrea Cimatti and Marshall Cohen for the important contribution they have made to the HzRG Keck II spectropolarimetry project from which some of the data herein comes. AH and PL acknowledge Fundação para a Ciência e a Tecnologia (FCT) support through UID/FIS/04434/2013, and through project FCOMP-01-0124-FEDER-029170 (Reference FCT PTDC/FIS-AST/3214/2012) funded by FCT-MEC (PIDDAC) and FEDER (COMPETE), in addition to FP7 project PIRSES-GA-2013-612701. AH also acknowledges a Marie Curie Fellowship co-funded by the FP7 and the FCT (DFRH/WIIA/57/2011), FP7 / FCT Complementary Support grant SFRH/BI/52155/2013, and FCT grant SFRH/BPD/107919/2015. PL is supported by a post-doctoral grant SFRH/BPD/72308/2010, funded by the FCT. Support for RO was provided by CNPq programs 459040/2014-6 and 400738/2014-7.

REFERENCES

- Adams J. J., Hill G. J., MacQueen P. J., 2009, *ApJ*, **694**, 314
 Allen M. G., Groves B. A., Dopita M. A., Sutherland R. S., Kewley L. J., 2008, *ApJS*, **178**, 20
 Arshakian T. G., Longair M. S., 2000, *MNRAS*, **311**, 846
 Asplund M., Grevesse N., Jacques Sauval A., 2006, *Nuclear Physics A*, **777**, 1
 Barkana R., 2004, *MNRAS*, **347**, 59
 Barkana R., Loeb A., 2003, *Nature*, **421**, 341
 Best P. N., Bailer D. M., Longair M. S., Riley J. M., 1995, *MNRAS*, **275**, 1171
 Best P. N., Carilli C. L., Garrington S. T., Longair M. S., Röttgering H. J. A., 1998, *MNRAS*, **299**, 357
 Bicknell G. V., Sutherland R. S., van Breugel W. J. M., Dopita M. A., Dey A., Miley G. K., 2000, *ApJ*, **540**, 678
 Binette L., Dopita M. A., Tuohy I. R., 1985, *ApJ*, **297**, 476
 Binette L., Kurk J. D., Villar-Martín M., Röttgering H. J. A., 2000, *A&A*, **356**, 23
 Bland J., Tully B., 1988, *Nature*, **334**, 43
 Carilli C. L., Perley R. A., Dreher J. W., Leahy J. P., 1991, *ApJ*, **383**, 554
 Carilli C. L., Röttgering H. J. A., van Ojik R., Miley G. K., Breugel W. J. M. van 1997, *ApJS*, **109**, 1
 Cepa J., et al., 2000, in Iye M., Moorwood A. F., eds, Proc. SPIE Vol. 4008, Optical and IR Telescope Instrumentation and Detectors. pp 623–631
 Cepa J., et al., 2003, in Iye M., Moorwood A. F. M., eds, Proc. SPIE Vol. 4841, Instrument Design and Performance for Optical/Infrared Ground-based Telescopes. pp 1739–1749, doi:10.1117/12.460913
 Christensen L., Jahnke K., Wisotzki L., Sánchez S. F., Exter K., Roth M. M., 2006, *A&A*, **452**, 869
 Dannerbauer H., et al., 2014, *A&A*, **570**, A55
 De Breuck C., van Breugel W., Stanford S. A., Röttgering H., Miley G., Stern D., 2002, *AJ*, **123**, 637
 De Breuck C., et al., 2010, *ApJ*, **725**, 36
 Dijkstra M., Haiman Z., Spaans M., 2006, *ApJ*, **649**, 14
 Douglas J. N., Bash F. N., Torrence G. W., Wolfe C., 1980, University of Texas Publications in Astronomy, **17**, 1
 Dubinski J., 1998, *ApJ*, **502**, 141
 Emonts B. H. C., et al., 2014, *MNRAS*, **438**, 2898

- Ferruit P., Binette L., Sutherland R. S., Pecontal E., 1997, *A&A*, **322**, 73
- Fosbury R. A. E., et al., 1982, *MNRAS*, **201**, 991
- Galametz A., et al., 2012, *ApJ*, **749**, 169
- Hatch N. A., Overzier R. A., Kurk J. D., Miley G. K., Röttgering H. J. A., Zirm A. W., 2009, *MNRAS*, **395**, 114
- Hatch N. A., et al., 2013, *MNRAS*, **436**, 2244
- Heckman T. M., 2003, in Avila-Reese V., Firmani C., Frenk C. S., Allen C., eds, *Revista Mexicana de Astronomia y Astrofisica Conference Series Vol. 17, Revista Mexicana de Astronomia y Astrofisica Conference Series*. pp 47–55
- Henry R. B. C., Edmunds M. G., Köppen J., 2000, *ApJ*, **541**, 660
- Humphrey A., Villar-Martín M., Fosbury R., Vernet J., di Serego Alighieri S., 2006, *MNRAS*, **369**, 1103
- Humphrey A., Villar-Martín M., Fosbury R., Binette L., Vernet J., De Breuck C., di Serego Alighieri S., 2007a, *MNRAS*, **375**, 705
- Humphrey A., Iwamuro F., Villar-Martín M., Binette L., Fosbury R., di Serego Alighieri S., 2007b, *MNRAS*, **382**, 1729
- Humphrey A., Villar-Martín M., Vernet J., Fosbury R., di Serego Alighieri S., Binette L., 2008a, *MNRAS*, **383**, 11
- Humphrey A., et al., 2008b, *MNRAS*, **390**, 1505
- Humphrey A., Iwamuro F., Villar-Martín M., Binette L., Sung E. C., 2009, *MNRAS*, **399**, L34
- Humphrey A., Binette L., Villar-Martín M., Aretxaga I., Papaderos P., 2013a, *MNRAS*, **428**, 563
- Humphrey A., Vernet J., Villar-Martín M., di Serego Alighieri S., Fosbury R. A. E., Cimatti A., 2013b, *ApJ*, **768**, L3
- Iwamuro F., et al., 2003, *ApJ*, **598**, 178
- Jarvis M. J., et al., 2001a, *MNRAS*, **326**, 1563
- Jarvis M. J., Rawlings S., Eales S., Blundell K. M., Bunker A. J., Croft S., McLure R. J., Willott C. J., 2001b, *MNRAS*, **326**, 1585
- Jarvis M. J., Wilman R. J., Röttgering H. J. A., Binette L., 2003, *MNRAS*, **338**, 263
- Klamer I. J., Ekers R. D., Sadler E. M., Hunstead R. W., 2004, *ApJ*, **612**, L97
- Legrand F., Kunth D., Mas-Hesse J. M., Lequeux J., 1997, *A&A*, **326**, 929
- Liu R., Pooley G., Riley J. M., 1992, *MNRAS*, **257**, 545
- Mayo J. H., Vernet J., De Breuck C., Galametz A., Seymour N., Stern D., 2012, *A&A*, **539**, A33
- McCarthy P. J., 1993, *ARA&A*, **31**, 639
- McCarthy P. J., van Breugel W., Spinrad H., Djorgovski S., 1987, *ApJ*, **321**, L29
- McCarthy P. J., Spinrad H., Dickinson M., van Breugel W., Liebert J., Djorgovski S., Eisenhardt P., 1990, *ApJ*, **365**, 487
- McCarthy P. J., Spinrad H., van Breugel W., 1995, *ApJS*, **99**, 27
- McCarthy P. J., Baum S. A., Spinrad H., 1996, *ApJS*, **106**, 281
- Miley G., De Breuck C., 2008, *A&ARv*, **15**, 67
- Nesvadba N. P. H., et al., 2009, *MNRAS*, **395**, L16
- Oke J. B., et al., 1995, *PASP*, **107**, 375
- Overzier R. A., Röttgering H. J. A., Kurk J. D., De Breuck C., 2001, *A&A*, **367**, L5
- Overzier R. A., Harris D. E., Carilli C. L., Pentericci L., Röttgering H. J. A., Miley G. K., 2005, *A&A*, **433**, 87
- Pentericci L., Röttgering H. J. A., Miley G. K., McCarthy P., Spinrad H., van Breugel W. J. M., Macchetto F., 1999, *A&A*, **341**, 329
- Pentericci L., Van Reeve W., Carilli C. L., Röttgering H. J. A., Miley G. K., 2000, *A&AS*, **145**, 121
- Pentericci L., McCarthy P. J., Röttgering H. J. A., Miley G. K., van Breugel W. J. M., Fosbury R., 2001, *ApJS*, **135**, 63
- Reuland M., et al., 2003, *ApJ*, **592**, 755
- Rocca-Volmerange B., Le Borgne D., De Breuck C., Fioc M., Moy E., 2004, *A&A*, **415**, 931
- Röttgering H. J. A., 1993, PhD thesis, Ph. D. thesis, University of Leiden (1993)
- Röttgering H. J. A., Lacy M., Miley G. K., Chambers K. C., Saunders R., 1994, *A&AS*, **108**, 79
- Röttgering H. J. A., Hunstead R. W., Miley G. K., van Ojik R., Wieringa M. H., 1995, *MNRAS*, **277**, 389
- Rush B., McCarthy P. J., Athreya R. M., Persson S. E., 1997, *ApJ*, **484**, 163
- Seymour N., et al., 2007, *ApJS*, **171**, 353
- Spearman C., 1904, *The Proof and Measurement of Association between Two Things*. University of Illinois Press, doi:10.2307/1412159
- Swinbank A. M., et al., 2015, *MNRAS*, **449**, 1298
- Tadhunter C. N., 1991, *MNRAS*, **251**, 46P
- Tadhunter C. N., Villar-Martín M., Morganti R., Bland-Hawthorn J., Axon D., 2000, *MNRAS*, **314**, 849
- Taniguchi Y., et al., 2001, *ApJ*, **559**, L9
- Tody D., 1993, in Hanisch R. J., Brissenden R. J. V., Barnes J., eds, *Astronomical Society of the Pacific Conference Series Vol. 52, Astronomical Data Analysis Software and Systems II*. p. 173
- Venemans B. P., et al., 2004, *A&A*, **424**, L17
- Vernet J., Fosbury R. A. E., Villar-Martín M., Cohen M. H., Cimatti A., di Serego Alighieri S., Goodrich R. W., 2001, *A&A*, **366**, 7
- Villar-Martín M., Tadhunter C., Clark N., 1997, *A&A*, **323**, 21
- Villar-Martín M., Tadhunter C., Morganti R., Axon D., Koeke-moer A., 1999a, *MNRAS*, **307**, 24
- Villar-Martín M., Binette L., Fosbury R. A. E., 1999b, *A&A*, **346**, 7
- Villar-Martín M., Fosbury R. A. E., Binette L., Tadhunter C. N., Rocca-Volmerange B., 1999c, *A&A*, **351**, 47
- Villar-Martín M., Fosbury R., Vernet J., Cohen M., Cimatti A., di Serego Alighieri S., 2001, *Astrophysics and Space Science Supplement*, **277**, 571
- Villar-Martín M., Vernet J., di Serego Alighieri S., Fosbury R., Pentericci L., Cohen M., Goodrich R., Humphrey A., 2002, *MNRAS*, **336**, 436
- Villar-Martín M., Vernet J., di Serego Alighieri S., Fosbury R., Humphrey A., Pentericci L., 2003, *MNRAS*, **346**, 273
- Villar-Martín M., Humphrey A., De Breuck C., Fosbury R., Binette L., Vernet J., 2007, *MNRAS*, **375**, 1299
- Willott C. J., Rawlings S., Blundell K. M., 2001, *MNRAS*, **324**, 1
- Wylezalek D., et al., 2013, *ApJ*, **769**, 79
- van Ojik R., 1995, PhD thesis, University of Leiden
- van Ojik R., Röttgering H. J. A., Miley G. K., Bremer M. N., Macchetto F., Chambers K. C., 1994, *A&A*, **289**, 54
- van Ojik R., Röttgering H. J. A., Miley G. K., Hunstead R. W., 1997, *A&A*, **317**, 358

This paper has been typeset from a $\text{\TeX}/\text{\LaTeX}$ file prepared by the author.